Project Title:	High-Temperature Linear Receiver Enabled by Multicomponent Aerogels
Project Period:	04/01/2021-06/30/2022
Project Budget:	
Submission Date:	09/30/2022
Recipient:	University of Michigan
Address:	2800 Plymouth Rd. Ann Arbor, MI 48104
Award Number:	DE-EE0009376
Principal Investigator:	Andrej Lenert Associate Professor of Chemical Engineering Phone: 734-647-4107 Email: alenert@umich.edu
Business Contact:	Colleen Vogler Senior Project Representative Phone: 734-647-2179 Email: clv@umich.edu
Technology Manager:	Matthew Bauer
Project Officer:	Christine Bing
Grant Specialist:	Laura Gonzalez
Contracting Officer:	Diana Bobo

Acknowledgement

This material is based upon work supported by the Department of Energy, Office of Energy Efficiency and Renewable Energy, Solar Energy Technologies Office, under Award Number DE-EE0009376.

Disclaimer

Uncertainty analysis:

Unless otherwise specified, uncertainty in the reported experimental quantities is evaluated through the propagation of the following errors: variance (using a t-distribution with a 90% confidence interval), instrument error, and resolution error. All errors were assumed to be uncorrelated. The number of distinct measured samples (N) is provided for reference.

Executive Summary

Concentrating solar thermal (CST) technology has significant potential mainly due to its dispatchability and low cost of storage. However, to compete with other sources, including utility-scale solar PV, its final cost (cents/kWh) still needs to be lowered. Cost reduction can be achieved by improving the system level efficiency of the CST plants through the deployment of advanced power cycles, which operate at high temperatures of ~700°C. However, optical, and thermal losses pose a major challenge to the efficiency of such CST systems.

The overall aim of this project is to investigate and de-risk a linear solar receiver concept called an Aerogel Insulated Receiver (AIR) that generates high temperatures (up to 700°C) at a low solar concentration ratio (<100) and with a high collection efficiency (optical × receiver). Our prior work has demonstrated the thermal stability[1] and optical and heat-insulating properties[2,3] of transparent aerogel insulation at a one-inch scale. The focus of this work is on (1) co-optimization of the geometry of the aerogel tile and receiver enclosure to fit a standard parabolic collector (PTC), (2) scale-up of aerogels into 4-inch tiles while preserving key properties, (3) experimental measurement of receiver heat loss (W/m) in a >70-cm test stand and validation of anticipated receiver performance at high temperatures.

Regarding (1), appropriate optical and thermal models for a parabolic trough receiver (PTR) are developed and validated. The geometry of the aerogels and the receiver enclosure are co-optimized to maximize the collection efficiency. The model predicts a 54% collection efficiency at 700°C for an AIR design based on flat aerogels. By combining the collection efficiency with the power block efficiency of supercritical CO_2 cycles, we predict >10% improvements in peak plant efficiency relative to existing line-focusing CST systems. The application of curved plasmonic aerogels is predicted to further increase the collection efficiency to 64%. Regarding (2), we demonstrate the successful development of 6-inch-long refractory aerogel tiles with optical, thermal, and stability characteristics consistent with our prior work. This scale-up requires a transition to a larger ALD station and modifying the ALD process variables such as exposure time and the number of precursor doses. Regarding (3), we design and develop an AIR test stand measuring 3 feet in length. Heat loss performance analysis is carried out using the test stand. The results indicate that aerogel insulation can significantly reduce receiver thermal losses at the high operating temperatures required for next-generation PTRs. The experimental results agree with the heat loss performance predicted by our receiver model. Lastly, we conducted preliminary failure mode and effects (FMEA) and techno-economic (TEA) analyses to identify failure mitigation strategies and commercial opportunities, respectively.

Overall, this project identifies key opportunities and challenges in deploying aerogel insulating receivers in next-generation line-focusing CST technologies.

Table of Contents

Background

Reaching high temperatures (700°C) using advanced solar receivers would enable the use of supercritical CO_2 (sCO_2) cycles, which operate at higher efficiency (~50%) and have lower capital costs than the currently used steam Rankine cycles.[4] High-temperature heat could also satisfy the energy demands of industrial processes that are particularly difficult to decarbonize.[5] Although many approaches are being pursued to reach this goal, parabolic troughs offer distinct advantages, including modularity and higher optical efficiencies compared to central receivers (~80% vs. <65%).[6,7] However, the lack of selective receivers that are robust to high temperatures presents a significant obstacle to deploying trough technologies that can drive sCO_2 cycles. Trough systems require selective receivers with high solar absorptance and low thermal emittance to maintain reasonable receiver efficiency. Selectivity is currently achieved by the application of thin optical coatings on durable, but otherwise not selective, materials such as metal alloys. These coatings undergo temperature-related degradation including oxidation, interdiffusion, and delamination which currently limits their use to temperatures below 650°C.[8] Overcoming this challenge would unlock the full potential of trough technologies and ultimately lead to large improvements in cost and reliability.

An alternative to selective coatings is transparent insulating materials (TIMs). Solar transmittance, thermal (infrared) opacity, and to a lesser extent, thermal conductivity are key properties of high-temperatures TIMs. In particular, radiative heat losses, which dominate at elevated temperatures, scale inversely with thermal opacity. Unfortunately, the thermal opacity and stability of existing TIMs are too low to achieve very high efficiency at ≥600°C. Silica aerogels, which are the leading TIMs, undergo densification and changes in surface chemistry at elevated temperatures that degrade their exceptional solar transmittance and heat-insulating properties,[9,10] making them unsuitable for next-generation applications. Specifically, they suffer from large radiative losses below 5 µm which accounts for ~63% of the blackbody emitted power at 700°C, mainly due to desorption of water and de-hydroxylation of IR-absorptive surface silanol groups. Even at the upper bound of practical aerogel thicknesses, losses through this window persist. In addition to becoming less insulating, silica aerogels become unstable above ~600°C. For example, after ~150 days at 700°C, silica monoliths shrink by ~75%.[10] Efforts to stabilize or reinforce the mesoporous structure of aerogels, which is essential to their spectral selectivity, have produced large compromises in transmittance and/or insulation.

To address these shortcomings, we created a refractory aluminum silicate surface through conformal atomic layer deposition (ALD), and we embedded nanoparticles that exhibit electromagnetic resonances in the infrared. Our efforts to date have established that these modifications stabilize the aerogel up to 800°C in air and selectively suppress heat losses by a factor of two.[1,2,11]

Our one-cycle UAR-ALD process using trimethylaluminum (TMA) and water achieves conformal coating of the internal pore structure of aerogel monoliths (>60:000:1). This would be extremely challenging to accomplish via alternative coating methods. Owing to the atomic-layer nature of

this process and the high surface area of the aerogels, this modification introduces a large fraction of aluminum into the solid phase (Si/Al ratio of 3:1) and creates a chemical bonding environment analogous to other thermally stable aluminum silicates.[11] The formation of this refractory ternary oxide prevents the loss of mesoscale porosity and preserves the shape of the aerogel monolith at 700°C in air. The modification also stabilizes the aerogel at temperatures as high as 800°C (in air) while maintaining exceptional optical and heat-insulating properties. Our ALD-modified aerogels achieved a 94% solar-weighted transmittance after aggressive aging at 800°C for >7 days.

We have also demonstrated an approach to suppress heat losses at 700°C to <10 Suns (<10 kW/m^2) by embedding IR-plasmonic ITO nanoparticles (NPs) within the aerogel matrix.[1,2] The result represents a five-fold reduction in heat losses relative to a blackbody emitter, and a two-fold reduction relative to pure silica aerogel. The approach, termed plasmon-enhanced greenhouse selectivity (PEGS), is particularly effective at high temperatures and has the added benefit of being air-stable, which contrasts favorably with existing selective coatings. Although embedding ITO NPs lowered the transmittance, we have identified the cause of this issue (particle agglomeration)[2] and should resolve it using a different NP ligand.

Although conformal ALD and PEGS have overcome key risks related to material properties, there remain several risks associated with further development of this technology. Namely, there is a risk that aerogel insulation will underperform when integrated into a realistic receiver geometry compared to model predictions based on planar, lab-scale configurations. There is also a substantial risk that the material properties will not be maintained when scaling to relevant sizes for integration with practical collectors. This SIPS project aims to address these critical risks.

Project Objectives

The objective of this SIPS project is to develop and de-risk a receiver technology with high collection efficiency ($\eta_{opt} \times \eta_{rec}$) by leveraging the high optical efficiencies characteristic of line-focusing systems (η_{opt} ~80%) and the high receiver efficiencies (η_{rec} ~80% @ 100 Suns) enabled by our ALD-coated aerogels. To achieve this goal, three milestones are defined as follows.

The first objective is the numerical co-optimization of HACA enclosure and aerogel where we simultaneously optimize the optical and receiver efficiency at high temperatures by varying the aerogel thickness, aerogel/aperture width, and rim/acceptance angle. The second objective involves the scale-up of aerogels and the associated manufacturing processes. In particular, the ALD process is re-optimized for larger aerogels by varying the deposition temperature, precursor partial pressures, and process sequence. To accelerate optimization, we leverage the knowledge acquired during our first SIPS project; specifically, an ALD process model that predicts coating penetration based on process parameters. The third objective is the integration of ALD-coated aerogel blocks into a 36-inch-long receiver and testing at 700°C. We build a 3-feet receiver test stand that is used to measure temperature-dependent thermal losses (under dark conditions) and evaluate thermal stability of the HACA receiver at 700°C.

Overall, the main project objectives can be described as:

- Develop and validate optical and thermal models for the collector
- Optimize aerogel insulated receiver geometry
- Scale up aerogels while preserving key material properties
- Confirm low degradation of solar transmittance of scale-up aerogels
- Analyze failure modes and mitigation strategies
- Validate insulation properties using a control receiver
- Evaluate heat loss performance of aerogel-integrated receiver using a test stand
- Analyze improvements in LCOE relative to commercially available systems

Project Results and Discussion

1. Numerical co-optimization of receiver enclosure and aerogel properties

Outcomes:

Developed and validated optical and heat loss models for a linear receiver.
Predicted a collection efficiency of 54% at 700°C. This improves the peak plant efficiency compared to lower temperature CST systems by >10% relative.
Pathways to 64% collection efficiency are proposed.

Milestone #	Performance Metric	Success Value	Assessment Tool / Method of Measuring Success Value	Verification Process	Additional Notes
1.1	**Relative Error** between UM Model and Baseline citations Collector optical and thermal models validated	**≤10% error** relative to a reference trough/LFR collector	**Max %**. **Instantaneous optical and receiver efficiency** used as measures of optical and thermal model accuracy, respectively. Comparisons to be made independently, whenever possible, and over all absorber temperatures and corresponding illumination conditions (e.g., polar angle) reported by the reference.	Reference systems include PTR70 and SunTrap. Report sent to DOE. Data format: Plot of modeled efficiencies vs measured efficiencies, for a given trough/LFR configuration and temperature. Include uncertainty estimate in model prediction at high T.	Direct comparison with reference to ≥550ºC, model output to ≥700ºC based on measured properties whenever available.
1.2	**Collection efficiency** for aerogel integrated receiver (AIR) where collection efficiency = instantaneous thermal energy collected by fluid divided by normal solar irradiance (per AM1.5D)	at least two AIR designs with >64% collection efficiency at 700ºC **Secondary objective: ≥10% improvement relative to a reference line focusing system** (nitrate salt; thermal oil, or steam based) of which at least one is suitable for detailed testing.	**Count**. Number of candidate AIR designs. **Sensitivity Analysis**. Accounting for uncertainty in material and system properties; design decisions; and discrete CSP systems. Discrete CSP systems may include select collectors, select HTF, and select power cycles determining inlet and outlet temperatures. **Relative improvement measured using overall plant efficiency** or LCOE, as calculated by SAM.	Report sent to DOE with description of design considerations. **Plot of efficiencies**, LCOE, and optimal AIR design parameters (thickness, width/arc, proximity to absorber) vs temperature, for a given trough/LFR configuration and absorber coating (black vs selective). Output SAM file. Output Component design file for a representative length of receiver (e.g., cad)	Efficiency, LCOE, and stability characteristics included in the report to assess the feasibility of the proposed design. AIR geometry optimized at each operating point. 64% is the product of an assumed 80% optical efficiency and 80% receiver efficiency

1.1. Optical modeling

We developed a model to estimate the performance of our novel refractory aerogel in linear solar concentrators using Soltrace (a Monte Carlo based ray tracing program created by NREL) and heat transfer models that combine radiation with conduction.

To design an aerogel insulated receiver, four different geometries for integration of aerogel into the receiver were considered (**Figure 1**). We have chosen to use opaque insulation to insulate the non-incident areas. In that regard, our design shares this similarity with the design proposed by Norwich Tech[12]. At temperatures > 400°C, the benefit of reduced thermal losses by using opaque insulation outweighs the loss of unconcentrated sunlight incident on the top of the receiver.

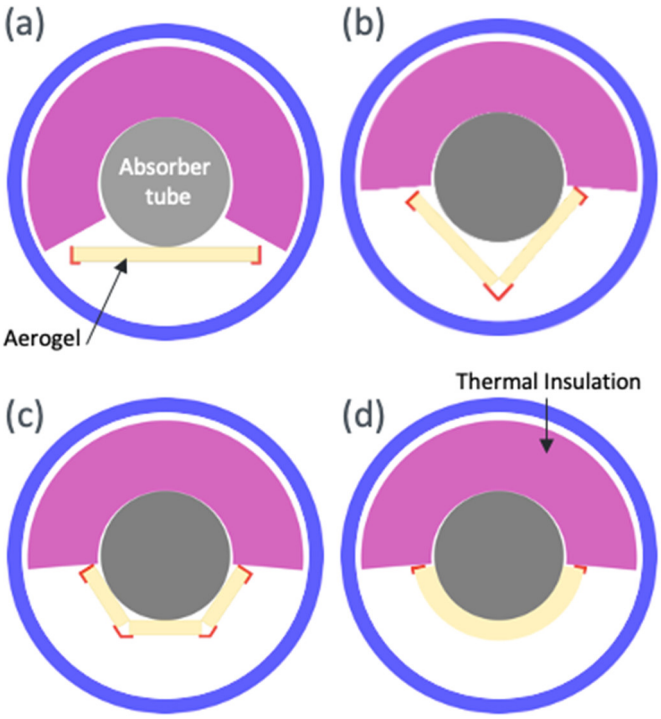

Figure 1. Four proposed geometries for aerogel integration into the receiver labeled as (a) flat, (b) V-shape, (c) half-hex, and (d) curved.

As shown in **Figure 1(a)**, the first configuration consists of a single stack of flat aerogel tiles placed along the tube length. While this geometry is favorable because of the simplicity it offers for receiver design, achieving an 80° acceptance angle with a single flat aerogel is impractical due to the very large glass envelope it would require. Hence, this geometry was discarded.

A V-shape aerogel configuration was another candidate in which two racks of aerogel tiles are positioned alongside each other to form a V-shape geometry below the absorber tube, as shown in **Figure 1(b)**. While still using flat aerogels, this geometry allows for large acceptance angles. It is also important that this geometry does not make the receiver design too complicated.

Half-hex is another proposed configuration where three racks of neighboring flat aerogel tiles are positioned to form a half hexagonal geometry below the absorber tube (**Figure 1(c)**). This design resembles the curved aerogel geometry more than the V-shape design and makes achieving large acceptance angles easier. However, it also adds complexity to the receiver design as the number of part increase. The required tracks to support the aerogel tiles also increase relative to the V-shape design which can result in additional shading.

Figure 1(d) shows the ideal curved geometry. However, our current aerogel synthesis capabilities are limited to flat aerogels, hence, this geometry was not selected for this project. Instead, we focus our analysis on the V-shaped and half-hex designs to elucidate which is most practical and feasible given our processing limitations. We analyze how the optical efficiency is affected by (i) longitudinal angle, (ii) latitudinal angle, and (iii) concentration ratio (**Figure 2**).

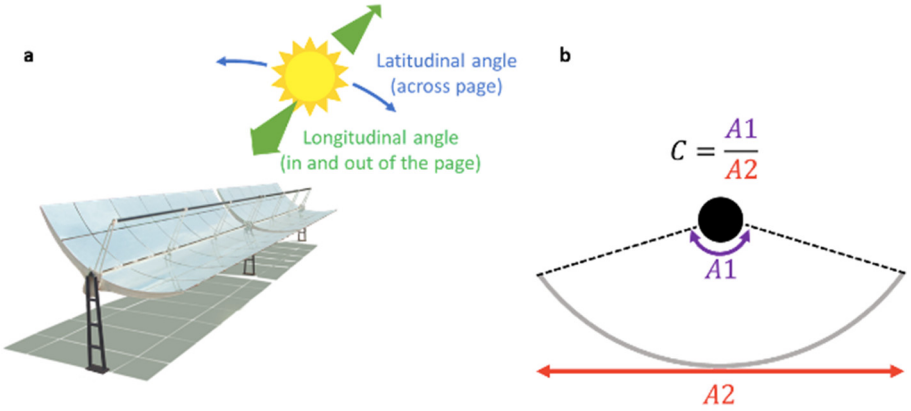

Figure 2. Independent variables of interest. (a) Linear receivers track across the latitudinal angle but are unable to track longitudinal angle. (b) The concentration ratio, C, is the ratio of the exposed area of the absorber to the projected area of the parabolic mirrors.

For linear concentrating systems, the latitudinal angle has a small impact on the optical efficiency (**Figure 3(a)**) because linear concentrators track the sun across the sky (i.e., latitudinally). At extreme latitudinal angles, however, neighboring concentrators block sunlight from reaching the mirrors of interest (**Figure 3(b)**). On the other hand, the longitudinal angle has a significant impact on the optical efficiency (**Figure 3(c)**). At locations far from the global equator or in certain seasons of the year, the sun follows an arc that is lower in the sky. As a result, any incident sunlight is off-normal which introduces cosine losses. Additionally, the ends of a receiver receive no concentrated sunlight due to the off-normal incidence (**Figure 3(d)**). Lastly, the optical efficiency decreases with increasing solar concentration ratio (**Figure 3(e)**). Most solar receivers are designed for an 80° acceptance angle, so the only way to increase the concentration ratio is to increase the projected area of the concentrating mirrors. Thus, the only way to increase the concentration ratio is to increase the focal length of the parabolic mirror. However, a higher focal length makes it more difficult for concentrated sunlight to reach the receiver due to focusing and surface errors (**Figure 3(f)**).

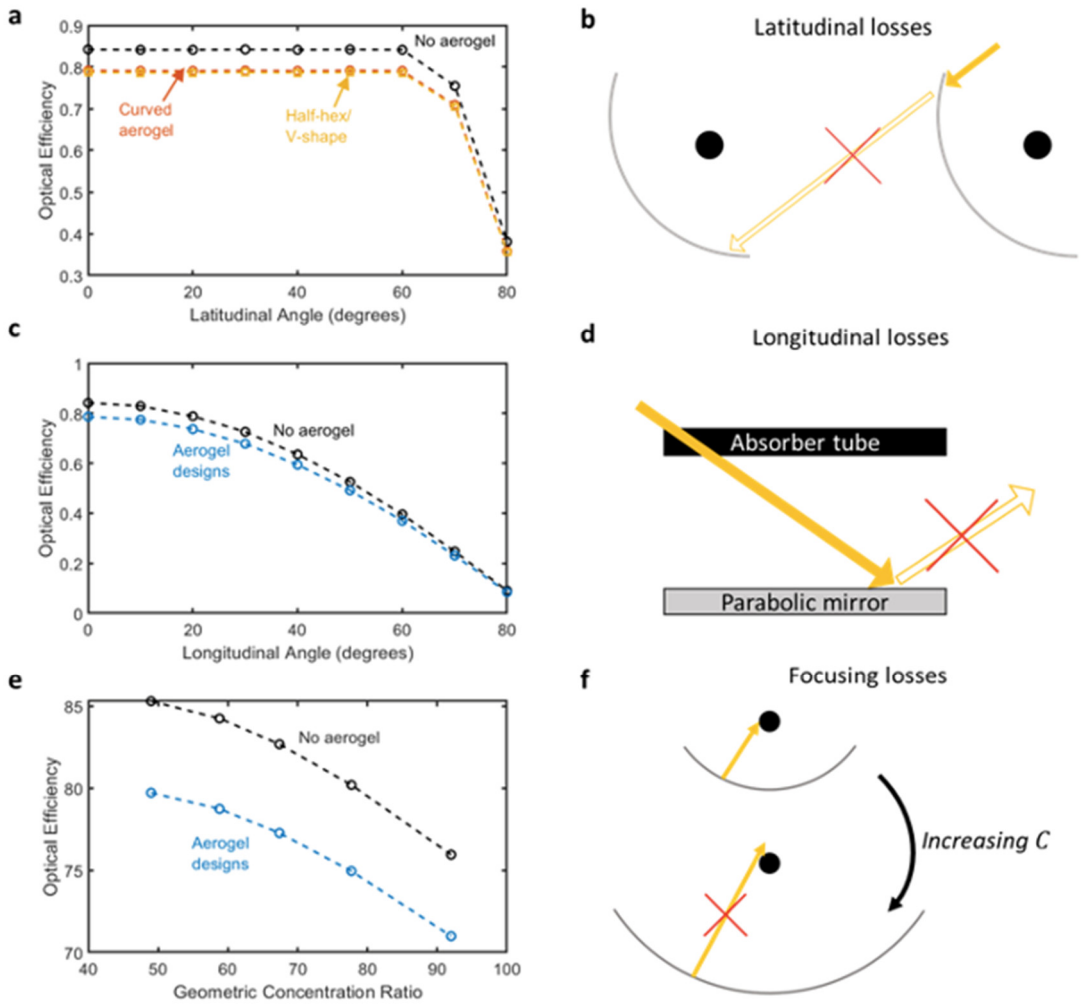

Figure 3. Results of the optical modeling: all aerogel designs have practically the same optical efficiency. (a), (b) Latitudinal losses only start at high incidence angles when neighboring troughs obstruct incident sunlight. (c), (d) Longitudinal losses are not only cosine losses, but also account for incident rays that miss the absorber tube. (e), (f) A ray that might be incident at a lower concentration misses at a higher one.

The optical efficiency modeling also shows that the curved aerogel indeed has the highest optical efficiency of any aerogel design followed by the half-hex design. Fortunately, the aerogels are highly transparent to normal incident light (94% solar-weighted transmission), such that the cosine losses from the V-shaped and half-hex designs are minimal. As a result, all three designs have nearly the same optical efficiency.

1.2. Heat loss modeling

The design has two regions, the opaque insulation, and the transparent cavity, where the heat losses occur through fundamentally different mechanisms. Thus, we treat these heat losses in parallel. If the transparent cavity only contains only a selective surface on the absorber tube, then we can treat radiation and convection within the tube in parallel as well. This resistance model is similar to a heat loss model for linear receivers developed by NREL[13]. To validate, we used inputs from Norwich Tech's previous report[12] on their SunTrap receiver designs (**Table 1**). Our results agree with Norwich Tech's experimental data well, thus providing confidence in our model. This model validation step, combined with the optical modeling reported above, **fulfills Milestone 1.1.**

Table 1. Comparison of resistance model to experimental results from Norwich Tech's report.

400 °C

Receiver Design	Experimental (W/m)	Resistance Model (W/m)	% Error
PTR70	230	231	**0.0**
SunTrap180	325	318	**2.1**

550 °C

Receiver Design	Experimental (W/m)	Resistance Model (W/m)	% Error
SunTrap180	580	605	**4.3**

Unlike selective surfaces, the heat losses associated with aerogels are much more complicated since aerogels since they consists of both radiative and conductive heat losses. To accurately estimate the heat losses through an aerogel-based receiver, the radiative transfer equation (RTE, Equation 1) needs to be solved simultaneously with the traditional heat transfer equation (HTE, Equation 2):

$$\frac{dI_\nu}{d\boldsymbol{s}} = -\beta_\nu I_\nu + (1-\sigma_\nu)\beta_\nu I_\nu + \frac{\beta_\nu \sigma_\nu}{4\pi}\int_{4\pi} I_\nu(\boldsymbol{s}_i)d\Omega_i \quad (1)$$

$$\nabla \cdot (k\nabla T) = \nabla \cdot q_r \quad (2)$$

The RTE is a computationally expensive equation to solve, so we break up the radiation spectrum into 25 distinct bands (**Figure 4(a)**). Additionally, our previous work has shown that our refractory aerogels have a temperature-dependent absorption in the infrared because of the strong hydrophilic nature of the surface aluminum group. We account for this phenomenon in this model. We also note that the model assumes the heat transfer occurs in a planar configuration (**Figure 4(b)**). Solving the RTE-HTE problem in cylindrical coordinates is not possible analytically, so we make a few adjustments to account for the cylindrical orientation in planar coordinates,

including using an effective emissivity for the glass tube that accounts for its larger area compared to if it was in a planar configuration.

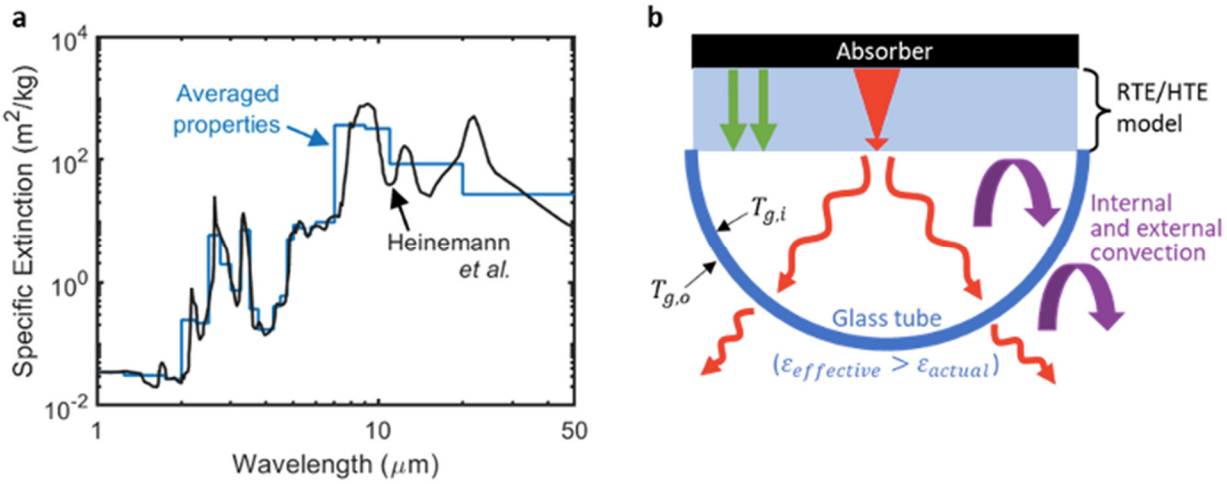

Figure 4. Heat transfer model and results for aerogel-based receivers. (a) The spectral properties of silica aerogels are averaged within 25 bands across the radiation spectrum. (b) The simulations model heat transfer in a planar (and not cylindrical) orientation. Additional measures are taken to adjust the values to reflect the cylindrical orientation more accurately.

1.3. Collection efficiency

The collection efficiency is a product of the receiver and optical efficiencies (Equation 3).

$$\eta_{\text{collection}} = \eta_{\text{receiver}} * \eta_{\text{optical}} \tag{3}$$

The optical efficiency of the receiver decreases with concentration ratio, but the receiver efficiency (Equation 4) increases with concentration ratio:

$$\eta_{\text{receiver}} = \tau - \frac{Q_{\text{loss}}}{CG_s} \tag{4}$$

where τ is the solar transmittance of the receiver, Q_{loss} is the heat lost, C is the concentration ratio, and G_s is the standard AM1.5D incident solar power (1,000 W/m^2). Thus, there will be a concentration ratio where the collection efficiency reaches a maximum.

Figure 5 shows that the aerogel receiver can achieve a collection efficiency of ~54% at 700°C when optimized. Losses are primarily due to relatively low optical efficiencies at the higher concentration ratios (e.g., 71% at 92 suns) and high thermal losses (~20 suns). Compared to state-of-the-art selective surfaces, however, the refractory aerogel performs significantly better.

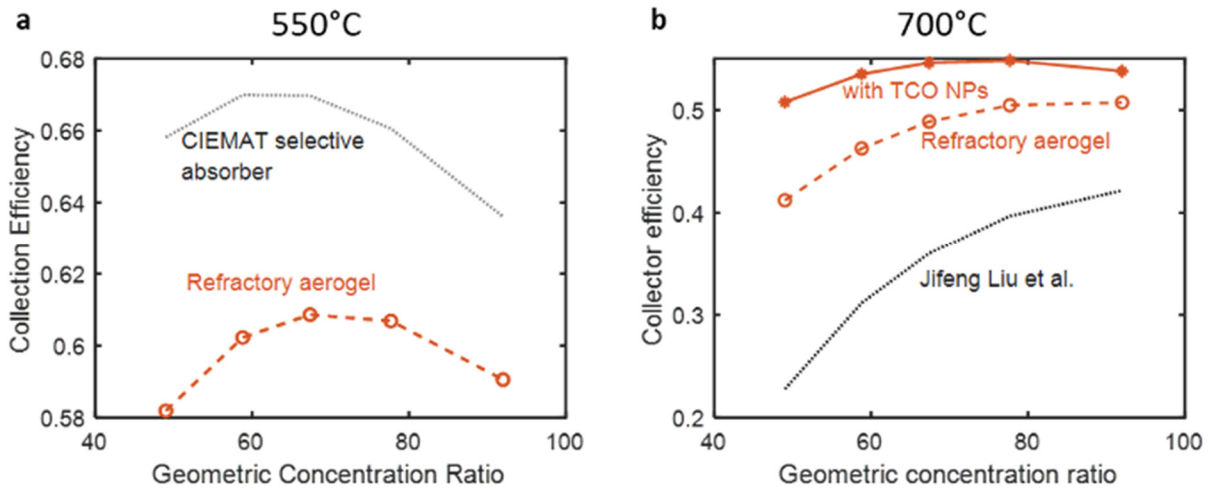

Figure 5. Collection efficiency for the curved aerogel configuration at (a) 550°C and (b) 700°C.

Figure 6 highlights the areas for improvement in the proposed receiver design. There are a few sources of improvement that we assume are out of the control of this project including losses from focusing spillage, optical shading, and mirror reflectance. The largest source of efficiency loss, however, is the heat loss. To mitigate these losses, we propose two options: increasing the thickness of the refractory aerogel, and (ii) incorporating infrared absorbing nanoparticles into the aerogel matrix. As demonstrated by the half-hex and V-shape designs, increasing the optical length of the refractory aerogel has little impact on solar transmission. Thus, we expect that we may be able to double the thickness of the aerogel without sacrificing much solar transmittance. Doubling the thickness is also expected to significantly decrease thermal losses. Alternatively, our previous work has shown that using indium tin oxide (ITO) nanoparticles can improve performance, but the transmission losses in that work were too high to improve performance in this application. A combination of these thermal reduction strategies and improvements in the transparency of the refractory aerogel is expected to result in collection efficiency of 64% at 700°C.

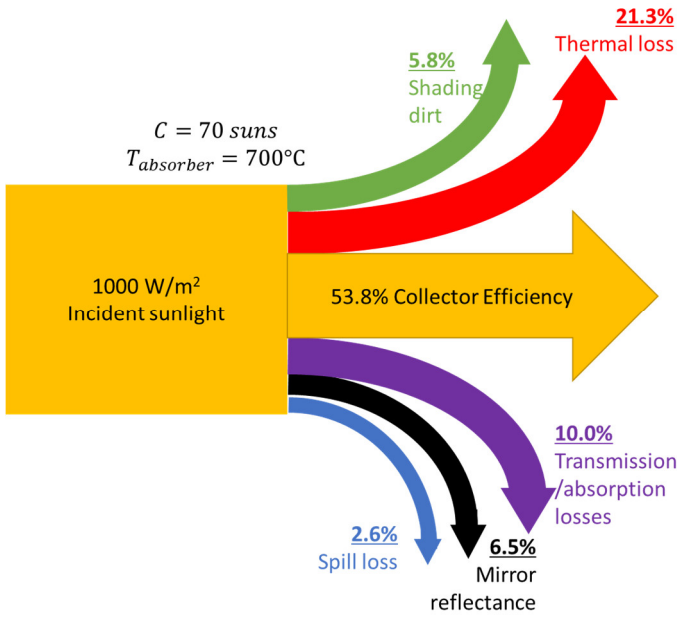

Figure 6. Schematic showing the sources of efficiency loss in the proposed receiver design at a concentration ratio of 70 suns and an absorber temperature of 700°C.

Summary:

When compared to state-of-the-art selective surfaces at 700°C, the refractory aerogel receiver is the most efficient design. The best selective surface, which is stable at 750°C in air, has a thermal emissivity over 50% and a solar absorptance of 92%. The refractory aerogel, on the other hand, has an apparent thermal emissivity of ~40% and a solar transparency of 96%, which leads to higher performance. The aerogel receiver design can in turn provide >10% improvement in peak power plant efficiency relative to a state-of-the-art line-focusing CSP plant (see **Table 2**), which **fulfills the secondary objective of Milestone 1.2.**

Table 2. Aerogel insulated receiver can improve peak plant efficiency by enabling higher operating temperatures.

Turbine inlet temp (°C)	Technology	Power cycle efficiency (%)	Collector efficiency (%)	Peak plant efficiency (%)
350	Selective surface	30-34[1]	70-73	**21.0-24.8**
550	Silica aerogel	42-46	62	**26.0-28.5**
700	Refractory aerogel	49-54	54	**26.5-29.2**

2. Scale-up of aerogels and manufacturing processes

Outcomes:
Scaled up 6” (long) refractory aerogel tiles exhibit comparable properties to initial 1” samples.

Milestone #	Performance Metric	Success Value	Assessment Tool / Method of Measuring Success Value	Verification Process	Additional Notes
2.1	**Solar transmittance; Apparent thermal emittance.** Key aerogel material properties achieved at the scale set by Milestone 1.2, but at least 10-cm wide and 0.3-cm thick	≥0.93 glass-enclosure-modified solar transmittance (tau), ≤0.26 apparent thermal emittance (e) based on measured heat loss Solution space may be updated based on learning from Milestone 1.2 **Constraints:** Absorber emittance ≥0.9, T ≥ 650ºC Aerogel aging: ≥650ºC for ≥48h in air	**Min tau/Max e** (average). Key materials properties measured using integrated UV-Vis-NIR and a custom heat loss stage. **Average** of ≥3 distinct ≥4-cm^2 samples taken from larger aerogel block. Measurement uncertainty ≤ 10% of average (90% confidence interval). **Experimental uncertainty propagation analysis.**	Report sent to DOE. Data format: spectral total transmittance (% vs. wavelength), temperature-dependent heat loss (kW/m^2).	Values were chosen to be **consistent with ≥80% efficiency for a planar (1D) receiver at 100 suns and 700ºC.**
2.2	**Degradation of solar transmittance and aerogel size** at scale (same as Milestone 2.1)	≤0.5% per 100 hours of operation in air at 700ºC	**Max %.** Averaged over a 10-day period following burn-in (~2 days). Acquisition frequency not to drop below every 2 days. **Function** describing degradation rate with appropriate fitting variable quantified (e.g., R^2). Fitting variable value should indicate moderate confidence the trend has been captured.	Report sent to DOE. Data format: solar transmittance and aerogel size as a function of aging time. Statistical evaluation of degradation-time functions, including linear & asymptotic.	Degradation rate was chosen based on prior work with 2.5-cm aerogels.

2.1. Development of scaled-up aerogel tiles

Large silica aerogel tiles were obtained from a commercial vendor (AeroShield Materials) for further fabrication and testing. The first set of aerogels had a relatively low density of ~60 kg/m^3, which was much lower than the density used in prior studies (defined here as the LD, or low density, samples). Our in-house heat transfer model suggests higher densities are more efficient because higher density aerogels are more insulating to radiation. Lower density aerogels, however, may be more effective at low (<300 °C) temperatures. The second set of aerogels had a density of ~140 kg/m^3 (defined here as the HD samples). In the following sections, we show a comprehensive analysis of the properties of the LD and HD aerogel tiles.

We note that we have only characterized two of each of the samples (i.e., N=2), rather three as outlined in our project goals, because of concerns of the limited number of useable samples. Nonetheless, all the aerogel tiles were synthesized in the same batch and cut into ~15cm x 7cm tiles. Therefore, the sample-to-sample variability should be negligible.

2.1.1. ALD recipe development and implementation

The aerogels tiles were coated with an ultrathin layer of alumina using atomic layer deposition (ALD). The ALD process was modeled using our previously published model[1], which was found to predict the conditions necessary for ALD infiltration to a certain depth with reasonable accuracy.

We transitioned to a different atomic layer deposition (ALD) instrument that is equipped with a larger deposition chamber to accommodate large-scale (~15 x 7 x 0.4 cm) aerogel tiles (**Figure 7**).

Figure 7. Picture of full-sized (~15.5 x 7 x 0.4 cm) tile in ALD chamber. Nuts are used to prop up the tile and facilitate diffusion of precursor to the bottom side of the tile.

We first calibrated the ALD process model that was developed during our first SIPS project to ensure good agreement between predicted and measured infiltration depths using aerogels fabricated at the University of Michigan, of which the properties (e.g., tortuosity, pore size, specific surface area, etc.) are known. As shown in **Figure 8**, the model was shown to fit well when varying the deposition conditions, namely the number of doses before dosing the counter

reactant and the exposure time. This shows that the ALD process model can be applied to other ALD instruments.

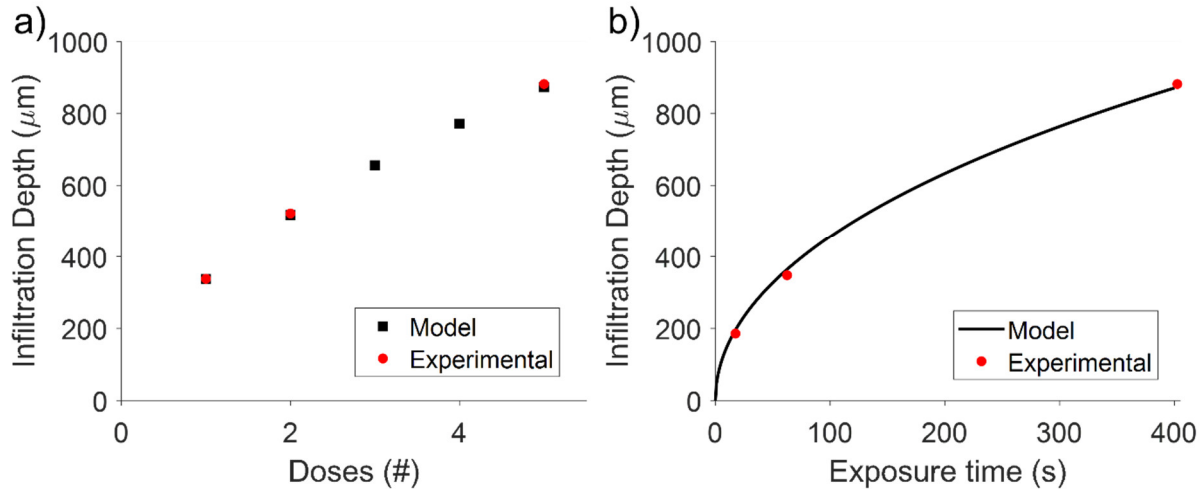

Figure 8. Modeled and experimentally measured infiltration depths of ALD on standard aerogel samples developed at University of Michigan. Depositions were performed using an ALD station with a larger deposition chamber.

The deposition conditions (number of doses before dosing the counter reactant and exposure time) were varied to calibrate the model for modifications of tiles. The only fitted parameter in this case was the tortuosity of the samples. Relatively small pieces (~1 x 1.5 x 0.4 cm) were modified to calibrate the model. Precursor infiltration occurred from each side of the samples. When comparing infiltration using the same deposition conditions on the top and bottom of the tile, one side was observed to consistently have deeper infiltration by ~10-15%. This could be due to variations in the properties of the aerogel through the sample cross-section. It is unlikely that this variation was due to external mass transport limitations, as the aerogel side with deeper infiltration faced downwards during the ALD process. Additionally, no variation in infiltration depth was observed with respect to x-y position on the tile, even in relatively large samples. When modeling infiltration into each side of the aerogel tile, there was reasonable agreement between the predicted and measured infiltrations (**Figure 9**).

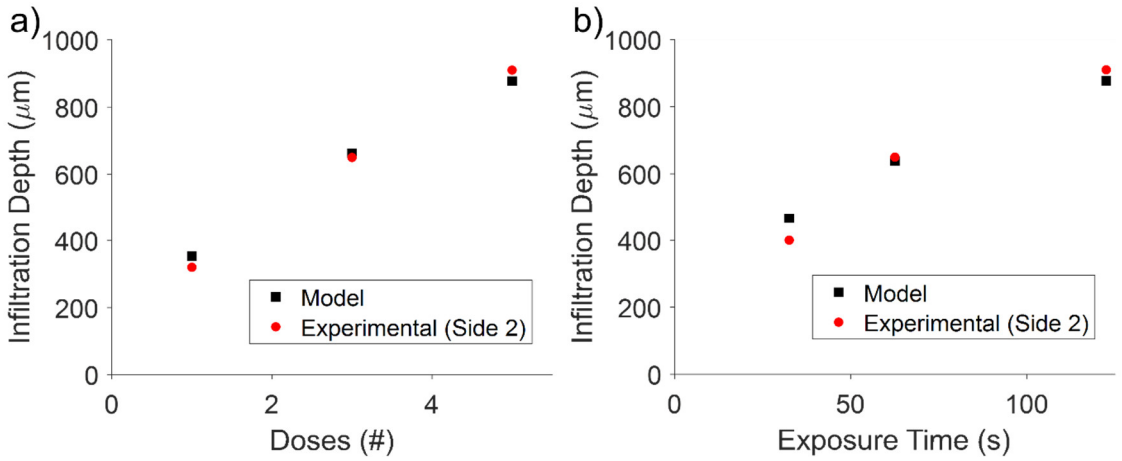

Figure 9. Modeled and experimentally measured infiltration depths of ALD on aerogel tiles. Depositions were performed using an ALD station with a larger deposition chamber.

Due to the limited number of usable samples, destructive scanning electron microscopy/energy-dispersive X-ray spectroscopy (SEM/EDS) analysis was performed on small pieces of the aerogel tiles (~2.5cm x 2.5cm). As shown in **Figure 10**, the ALD modification was relatively conformal. The mass gain following the ALD process in these small samples was ~23%, which was similar to the predicted value when taking into account the ALD thickness and density, as well as the specific surface area. ALD coatings on the full-scale (15cm x ~7cm) tiles showed mass gains of ~24%. This agreement provides reasonable confidence that the ALD modification is conformal without the need for destructive SEM/EDS analysis. Additionally, there were no visible signs of a partial coating infiltration, which can generally be seen by eye.

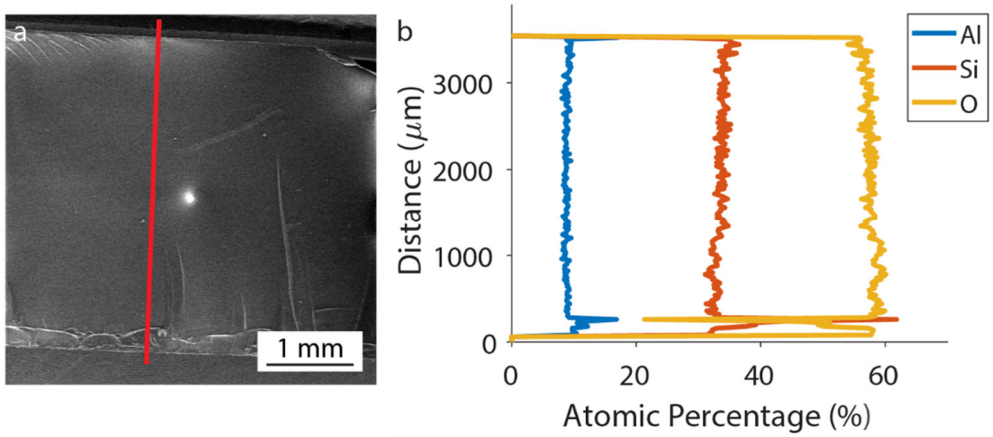

Figure 10. (a) SEM image and (b) EDS line-scan of samples. The noise at low "distance" values is due to the rough surface in the cross-section at that location.

2.1.2. Demonstration of key aerogel properties at scale

Thermal stability:

We repeated a thermal stability study found in our previous publication[3] that measured the linear shrinkage of aerogel samples after 1, 2, 4, 7, and 10 days of annealing at 700°C in air (**Figure 11(a)**). We show that the uncoated LD samples are less stable than our reference uncoated samples. However, the ALD alumina coating introduces a similar level of thermal stability compared to our reference coated samples. Both the coated reference and coated LD samples show a plateau of degradation, while the uncoated LD samples are not stable at 700°C. Specifically, the degradation rate of the coated LD samples is 0.46 $\pm$ 25% per 100 hours after the initial 'burn-in' period. This value meets the project goal of 0.5% per 100 hours, which combined with solar transmittance values shown below, **fulfills Milestone 2.2**.

Figure 11(b) shows that the HD samples have even greater thermal stability thus far in the analysis. After 10 days of annealing at 700°C, the HD samples shrank only 6.9 ± 0.2% compared to 10.15 ± 0.5% for the LD. The asymptotic degradation of the rate of the aerogels is slightly lower compared to the LD at 0.41 ± 0.08% per 100 hours, further demonstrating the greater stability for the HD samples.

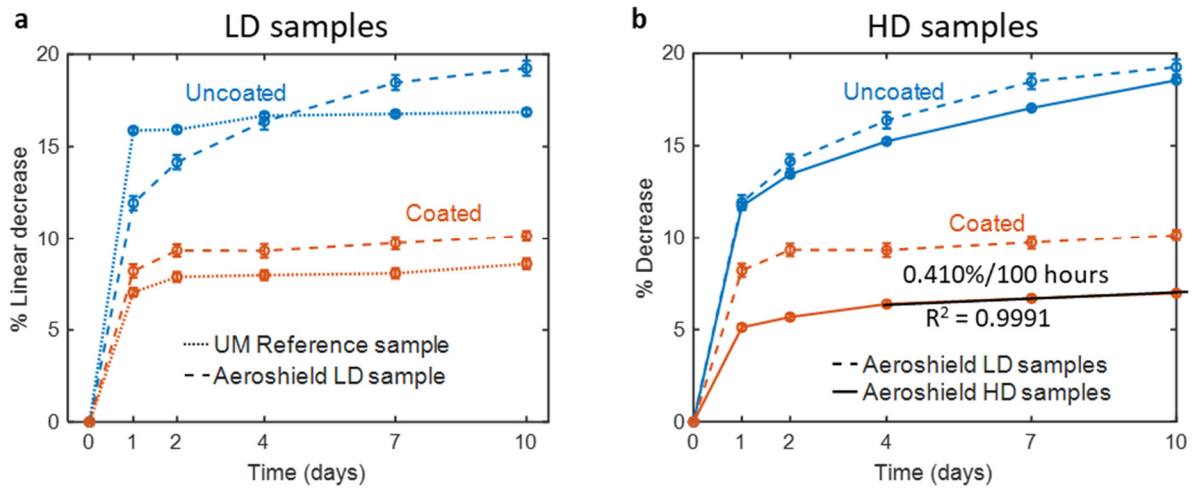

Figure 11. Thermal degradation of uncoated and coated aerogels. (a) Comparison of LD samples (dashed lines) to the University of Michigan reference samples (dotted lines). (b) Comparison of LD (dashed lines) and HD (solid lines) samples.

Solar transmittance:

Both the LD and HD aerogel tiles demonstrate very high solar-weighted transmittance (SWT) (**Figure 12**). Specifically, the LD and HD samples have SWT of 97.9% and 97.6%, respectively. After aging at 700°C, however, the transmittance of the uncoated samples decreased. For the LD samples, the SWT decreases from 97.9% to 96.6% after annealing at 700°C for 7 days. After an additional 3 days at 700°C, we then annealed the samples for 2 days at 800°C to test their stability at more aggressive conditions. The uncoated LD samples showed continued degradation in SWT, decreasing to 95.1%. On the other hand, the coated LD samples showed greater resilience by also decreasing to 95.1%, but it is still nearly 2% higher than their initial transparency of 93.5%.

The HD aerogels demonstrate similar behavior in SWT. After annealing at 700°C for 10 days, the SWT of the uncoated HD samples decreased to 95.5%. The coated HD samples, on the other hand, increased to 95.6%, which is higher than the uncoated samples. The asymptotic degradation of the transmittance of the HD samples is 0.186 ± 0.285%/100 hours, which is again below the project goal of 0.5%/100 hours.

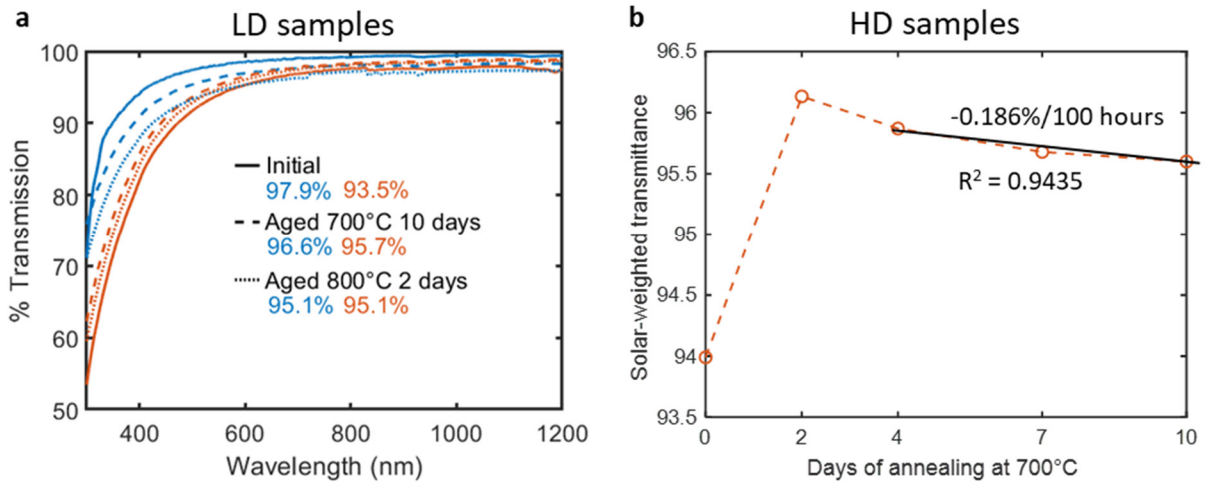

Figure 12. Solar transmittance of aerogel tiles. (a) Effect of annealing conditions on the solar-weighted transparency of the tiles. The densification of the uncoated samples leads to greater scattering and reflectance. (b) Effect of annealing on the solar-weighted transmittance of the coated HD samples.

Thermal insulation:

To confirm that the commercial aerogel tiles exhibit similar insulating properties to the University of Michigan reference samples, we repeated heat flux measurements from our previous project (**Figure 13**). However, there was an issue with the heat flux sensor because it exhibited a different sensitivity compared to its prior use in January of 2021. We therefore re-calibrated the sensor using a standard experiment whereby we measure the heat fluxes with no insulation. The sensor's sensitivity changed by 30%, so we use the updated sensitivity of the heat flux sensor for all experimental measurements here. We first confirmed the accuracy of the updated sensor sensitivity by re-measuring the heat losses of a reference uncoated aerogel developed at the University of Michigan. The results agree, predicting a heat loss of 15.3 ± 0.5 kW/m^2 (ε_{app}=0.301 ± 0.010), compared to a previously measured value of 16.3 ± 0.6 kW/m^2 (ε_{app}=0.321 ± 0.012). Comparing the heat losses of the uncoated LD aerogel tiles, we see the heat flux is about 15% higher (18.2 ± 0.6 kW/m^2) than the University of Michigan reference sample which is expected since the LD sample has a much lower density (60 compared to 170 kg/m^3). This result, combined with the solar transmittance reported above, **fulfills Milestone 2.1.**

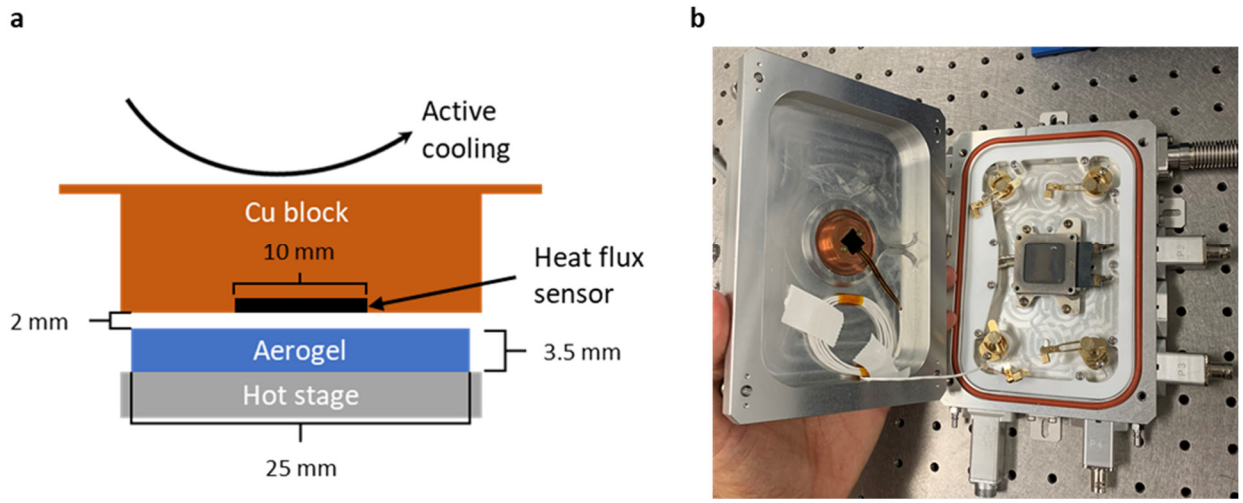

Figure 13. Heat flux measurement setup. Schematic (a) and picture (b) of the heat flux setup. A commercially available heat flux sensor is integrated into an actively cooled copper block. A hot stage is pumped under vacuum and an aerogel is placed between the copper block and the hot stage. The heat flux is recorded via a voltage from the heat flux sensor.

Summary:

Table 3 shows the summary of relevant properties of the coated aerogels. The solar-weighted transmittance of the HD tiles, after 240 hours of annealing at 700°C, is 95.7 ± 1.0 %. The transmittance is 2% higher than that of our reference small aerogels (93.7%). The heat loss properties of the tiles and small reference aerogels are comparable. The apparent emittance of the LD tile is estimated to be 5% higher than the reference sample, which is expected due to its much lower density. Lastly, the asymptotic degradation rates of both the LD and HD tiles are within the project goals, suggesting the ALD process is broadly applicable to silica aerogels. This study confirms that scaling up the ALD coating process to larger aerogel tiles can maintain desirable properties.

Table 3. Overview of aerogel tile properties

	LD Tile	HD Tile	1" Reference
Solar transmittance (%) (post-aging)	95.7 ± 1.1	95.6 ± 1.0	94.0 ± 1.0
Transmittance loss (%/100h)	-	0.19 ± 0.3	0.08 ± 0.1
Shrinkage (%) (post-aging)	10.2 ± 0.3	6.9 ± 0.1	8.6 ± 0.3
Shrinkage rate (%/100h)	0.46 ± 0.25	0.41 ± 0.08	0.36 ± 0.3
Apparent emittance (700°C)	0.36 ± 0.01	0.31 ± 0.01	0.30 ± 0.01

2.2. Failure modes and effect analysis

Outcomes:
FMEA is performed and potential failure modes and mitigation strategies are listed.

Milestone #	Performance Metric	Success Value	Assessment Tool / Method of Measuring Success Value	Verification Process	Additional Notes
2.3	Failure modes and mitigation strategies analyzed	Identification of single failure points and system interface problems, which may be critical to mission success and/or safety.	**Failure mode and effects analysis (FMEA).** Two cases considered (i) on-sun testing of AIR in a trough system, and (ii) general considerations for a MW-scale, 30-year lifetime plant. At least 2 external stakeholders executing FMEA exercise (e.g., CSP experts, thermal systems experts, aerogel manufacturing experts).	Report sent to DOE.	Experienced FMEA team, approved by DOE.

To further substantiate our aerogel insulated receiver design, a Failure Mode and Effect Analysis (FMEA) was conducted. The objective of the FMEA was to recognize the potential failure mechanisms of our design and the corresponding mitigation strategies. The scope of our analysis was around the aerogel. Its interactions with outside components are defined in the boundary diagram, **Figure 14.**

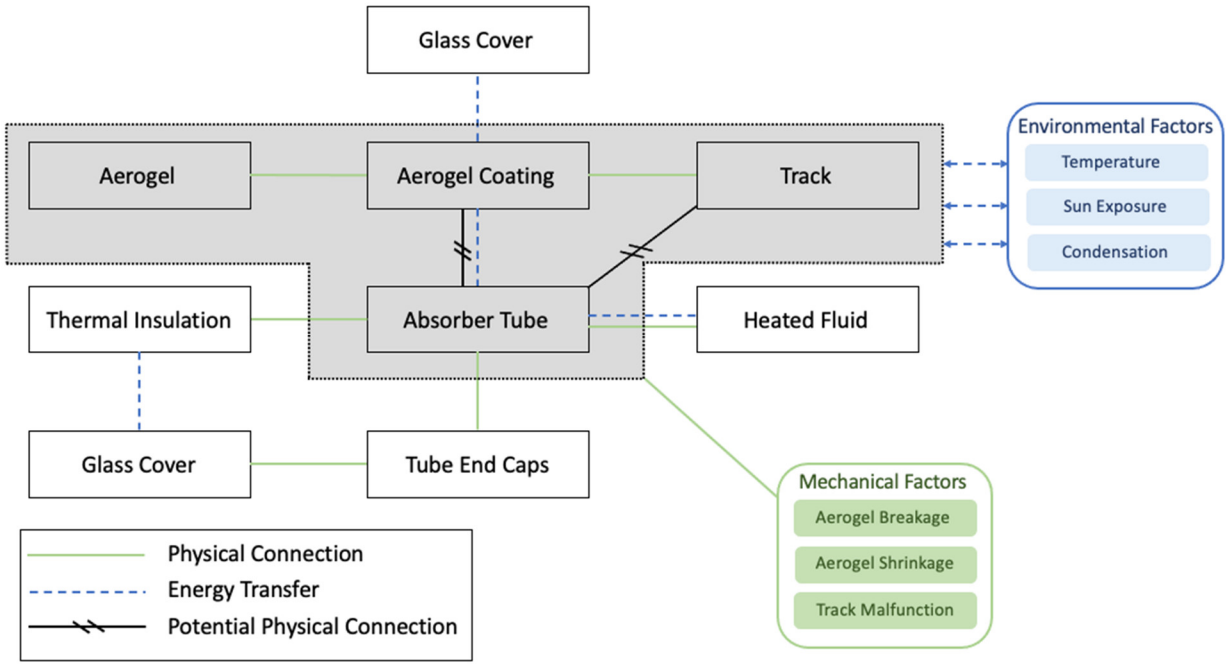

Figure 14. Boundary diagram drawn to analyze the failure modes of aerogels.

The first section of the FMEA table is the Function Description consisting of three parts: the input, action, and output. As shown in **Table 4,** for our design the input is the flow of warm fluid into the tube, the action is heating up the fluid, and the measurable output is the recorded temperature difference and flow rate.

Table 4. FMEA Function Description.

Function Description		
Input/ Assumptions	**Verb/ Noun**	**Measurable Output**
Warm fluid in tube from low to high	Heat up	Temperature difference and flow rate

In the second section, we identified the Potential Failure Modes of our design and the resulting effects. As shown in **Table 5**, the two potential failure modes for an aerogel are: 'Lack of solar absorption' and 'Lack of heat insulation'. In either case, the effect on the overall design is 'Underperformance'.

Table 5. FMEA Function Description.

Failure Mode	
Potential Failure Mode	**Potential Effects**
Lack of solar absorption	Underperformance
Lack of heat insulation	

The third section covers the 'Mechanisms of Failure' for each mode and the corresponding 'Potential Causes'. In our analysis we present all conceivable events that we believe could lead to an instance of failure. The potential mechanisms and causes of failure that can lead to a 'Lack of solar absorption' or a 'Lack of heat insulation' are shown in **Table 6** and **Table 7**, respectively. Please note that the cells highlighted in blue indicate failures associated with components outside of the main boundary in our system boundary diagram.

After discussing the circumstances in which our design could fail, we then identified the actions that could prevent these modes from ever occurring. The fourth section, Current Design Controls, provides both a preventative Design Method and Product Characteristic. See **Table 6** and **Table 7**. Next, methods of detecting the failure mode/mechanism were identified. If a failure mode was present in our design, the method of conducting a virtual Check would be the remote 'temperature measurement sensor', while the option for Physical Test is limited to 'visual inspection'.

Additionally, within the FMEA table there is a list of different parameters such as the severity of impact of a potential failure mechanism (SEV), the likelihood of occurrence (OCC) and detectability (DET). These values were assigned on a scale of 1-10.

SEV establishes how critical the impact of each potential failure mechanism could be. A ranking of 10 is defined as 'Hazardous without warning' while a ranking of 1 is defined as 'No discernible effect'. As an example, in **Table 7** the failure mechanism 'Gaps between aerogels' was assigned a SEV of 5 as the design would remain operable but at a reduced rate of performance.

OCC describes the likelihood that each failure mechanism will occur during the design life. An OCC of 1 means the 'failure is eliminated through preventative control', while a ranking of 10 means that the failure has a likelihood of occurring greater than 1 in 10. As an example, in **Table 6** the failure mechanism 'Irregular thickness of aerogels' was assigned an OCC of 1 as it can be prevented by the use of 'high quality flat molds'.

DET explains how effective a detection method is for a given failure mechanism. A rank of 1 is given if the likelihood of detection is 'almost certain' or if the failure mechanism 'cannot occur because it is fully prevented through design solutions'. A rank of 10, however, means it is 'almost impossible' to detect the failure mechanism. As an example, in **Table 6** the failure mechanism 'Cracks in aerogel' was given a DET of 9 because it would be 'almost impossible' to detect via a 'Temperature measurement sensor' or 'visual inspection'.

Finally, to assess the overall risk of each potential failure cause, an all-encompassing risk priority number (RPN) was assigned, being the product of SEV, OCC, and DET. The full FMEA table is provided in **Table 8**.

Table 6. Mechanisms and Causes of Failure and Current Design Controls for Lack of Solar Absorption.

Mechanisms and Causes of Failure				Current Design Controls						
				Prevention			Detection/ Verification			
SEV	Mechanisms of Failure	Potential Causes		Design Methods	Product Characteristics	OCC	Virtual Check	Physical Test	DET	RPN
6	Low aerogel transparency	Shading by track		N/A	Use of transparent or triangular track				9	162
		Surface contamination of volatile species		Test the effect of volatile species on aerogel surface	Use Ammonia: Silica Precursor ratio from Zhao et al. ACS Nano. 2019.	3				
				Prevent the condensation of volatile species in tube						
6	Poor absorption of solar absorbing coating	Coating degradation		Reapply the coating within its lifespan	Use high temperature stable absorbing coating	5			9	270
6	Increased opacity of tube	Degradation of black coating		Regular maintenance cleaning for dust and other particulate removal	Pre-anneal the tube to ensure particulates do not come in contact with aerogel surface or glass envelope	1			9	54
					Use antidust and/or hydrophobic coatings					
6	Degradation of glass envelope	Weather		Regular maintenance and cleaning	Use high quality glass	1	Temperature measurement sensor	Visual Inspection	1	6
2	Cracks in aerogels	Thermal shock and expansion		Store in mechanically stable environment	Shock-resistant receiver design	8			9	144
		Vibration		Stress test aerogel under multiple vibration frequencies	High quality aerogels (no pre-existing cracks)					
2	Irregular thickness of aerogels	Manufacturing defects		Inspect aerogels for discrepencies in thickness	Use high quality, flat aerogel molds	1			1	2
7	Deterioration of aerogel	Exposure to high temperature cycling		Store in mechanically stable environment	Use aerogels with conformal and uniform ALD coating	4			8	224
				Test long-term aerogel exposure to high temperature cycling						
		Exposure to moisture		Store under vacuum	Use pre-annealed aerogels					
		Wear from track contact		Simulate aerogel/track interface with long term thermal cycling, validate with experimentation	Use mounting that minimizes contact and accomodates aerogel expansion and contraction					

Table 7. Mechanisms and Causes of Failure and Current Design Controls for Lack of Heat Insulation

	Mechanisms and Causes of Failure			Current Design Controls							
				Prevention			Detection/ Verification				
	Mechanisms of Failure	Potential Causes		Design Methods	Product Characteristics	OCC	Virtual Check	Physical Test	DET	RPN	
5	Gaps between aerogels	Mechanical degradation of aerogels		Horizontal compression mechanism to adjust for any shrinkage	Use pre-annealed aerogels		Temperature measurement sensor	Visual Inspection	9	180	
5		Aerogel shrinkage			Design excess coverage of aerogels such that any shrinkage will not be exposed to glass	4					
2	Cracks in aerogels	Thermal shock and expansion		Store in mechanically stable environment	Shock-resistant receiver design and high quality aerogels with no pre-existing cracks	8			9	144	
2		Environmental changes		Store under vacuum							
5	Increased conductivity of aerogels	High temperature sintering		Store in mechanically stable and dry environment	Use aerogels with conformal and uniform ALD coating	1			1	5	
5		Degradation over time with use									
2	Non-ideal geometry of aerogels	Manufacturing defects		Inspect aerogels for defects and shrinkage/degradation	Curved aerogel design	1			1	2	
2		Aerogel shrinkage/degradation			Use track that supports the shrinkage/degradation of curved aerogel						
7	Track Failures (breaking)	Track degradation		Perform periodic tests to ensure mechanical robustness		1			1	7	
7	Track Malfunctioning	Exposure to high temperature cycling		Simulate cycling to test interface between track and track supports, validate with experimentation	Use high temperature stable metal supports (Inconel or stainless steel)	1			1	7	

Table 8. Full FMEA Table

Function Description			Failure Mode		Mechanisms and Causes of Failure			Current Design Controls					
								Prevention		Detection/Verification			
Input/ Assumptions	Verb/ Noun	Measureable Output	Potential Failure Mode	Potential Effects	SEV	Mechanisms of Failure	Potential Causes	Design Methods	Product Characteristics	OCC	Virtual Check	Physical Test	DET	RPN
							Shading by track	N/A	Use of transparent or triangular track					
					6	Low aerogel transparency	Surface contamination of volatile species	Test the effect of volatile species on aerogel surface	Use Ammonia: Silica Precursor ratio from Zhao et al. ACS Nano. 2019.	3			9	162
								Prevent the condensation of volatile species in tube						
					6	Poor absorption of solar absorbing coating	Coating degradation	Reapply the coating within its lifespan	Use high temperature stable absorbing coating	5			9	270
					6	Increased opacity of tube	Degradation of black coating	Regular maintenance cleaning for dust and other particulate removal	Pre-anneal the tube to ensure particulates do not come in contact with aerogel surface or glass envelope	1			9	54
									Use antidust and/or hydrophobic coatings					
					6	Degradation of glass envelope	Weather	Regular maintenance and cleaning	Use high quality glass	1	Temperature measurement sensor	Visual Inspection	1	6
					2	Cracks in aerogels	Thermal shock and expansion	Store in mechanically stable environment	Shock-resistant receiver design	8			9	144
							Vibration	Stress test aerogel under multiple vibration frequencies	High quality aerogels (no pre-exisiting cracks)					
					2	Irregular thickness of aerogels	Manufacturing defects	Inspect aerogels for discrepencies in thickness	Use high quality, flat aerogel molds	1			1	2
					7	Deterioration of aerogel	Exposure to high temperature cycling	Store in mechanically stable environment	Use aerogels with conformal and uniform ALD coating	4			8	224
								Test long-term aerogel exposure to high temperature cycling						
							Exposure to moisture	Store under vacuum	Use mounting that minimizes contact and accomodates aerogel expansion and contraction					
							Wear from track contact	Simulate aerogel/track interface with long term thermal cycling, validate with experimentation	Use pre-annealed aerogels					
					5	Gaps between aerogels	Mechanical degradation of aerogels	Horizontal compression mechanism to adjust for any shrinkage	Design excess coverage of aerogels such that any shrinkage will not be exposed to glass	4			9	180
							Aerogel shrinkage		Use pre-annealed aerogels					
					2	Cracks in aerogels	Thermal shock and expansion	Store in mechanically stable environment	Shock-resistant receiver design and high quality aerogels with no pre-existing cracks	8			9	144
							Environmental changes	Store under vacuum						
					5	Increased conductivity of aerogels	High temperature sintering	Store in mechanically stable and dry environment	Use aerogels with conformal and uniform ALD coating	1			1	5
							Degradation over time with use							
					2	Non-ideal geometry of aerogels	Manufacturing defects	Inspect aerogels for defects and shrinkage/degradation	Curved aerogel design	1	Temperature measurement sensor	Visual Inspection	1	2
							Aerogel shrinkage/degradation		Use track that supports the shrinkage/degradation of curved aerogel					
					7	Track Failures (breaking)	Track degradation	Perform periodic tests to ensure mechanical robustness	Use high temperature stable metal supports (Inconel or stainless steel)	1			1	7
							Exposure to high temperature cycling	Simulate cycling to test interface between track and track supports, validate with experimentation						
					7	Track Malfunctioning				1			1	7

3. Integration and testing of aerogel tiles in a prototype receiver

Outcomes:
Developed and tested a 90-cm-long aerogel insulated receiver.
Experimental heat loss results agree with model predictions after accounting for absorber tube temperature profile and receiver edge losses.
Aerogel insulated receiver reduces thermal losses by more than 50% at 700°C.
Thermal loss tests are carried out with a measurement uncertainty of <5%.

Milestone #	Performance Metric	Success Value	Assessment Tool / Method of Measuring Success Value	Verification Process	Additional Notes
3.1	**Thermal Loss Uncertainty** Experiment validation: Direct insulation measurement built and validated using control receiver (no aerogel)	Uncertainty: **≤10% of average** (90% confidence interval) Absorber T ≥ 700ºC	**Max %/Min ºC**. Measure linear heat losses versus absorber temperature. **Uncertainty propagation analysis**. At least 5 measurements at each T.	Report sent to DOE. Data Format: linear heat loss (W/m) vs. temperature, uncertainty propagation analysis, record of any observed failures.	Receiver to measure ≥70 cm in length.
3.2	**Thermal Loss** & Thermal Loss Uncertainty	**Within 5 percent of Loss Set by Milestone 1.2.** **Uncertainty**: ≤10% of average (90% confidence interval) Absorber T ≥ 700ºC	**Max %/Min ºC**. Measure linear heat losses versus absorber temperature. At least 5 measurements at each T. At least 3 heating/cooling cycles. **Uncertainty propagation analysis.**	Report sent to DOE. Data Format: linear heat loss (W/m) vs. temperature, uncertainty propagation analysis, record of any observed failures.	Receiver to measure ≥70 cm in length.

3.1. Development of direct insulation test stand

A 36-inch-long receiver test stand is designed and developed, where an absorber tube with a length of 36 inches (~91 cm) resides inside a 120 cm long quartz tubular envelope.

The design incorporates a combination of transparent and opaque thermal insulations to cover the absorber tube. In fact, since in a commercial PTR, concentrating mirrors with a rim-to-rim angle of 160° will be located below the receiver, we designed the receiver so that the aerogels cover a 160° angle of the lower circumference of the tube. This angle corresponds to an 80° acceptance angle. Opaque thermal insulation can be used to cover the remainder of the circumference of the tube, in which the incoming solar irradiation is negligible. **Figure 15** demonstrates a conceptual design for the aerogel-integrated receiver.

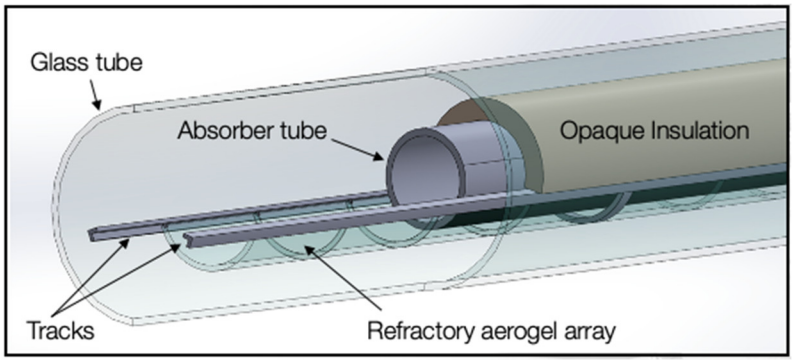

Figure 15. Schematic of the original 36-inch-long receiver test stand design where opaque and transparent insulations are integrated into the PTR design.

Due to the challenges associated with the fabrication of curved aerogels, we investigated alternative designs that could use flat aerogel tiles to approximate the desired curvature. A V-shape configuration where two arrays of flat aerogel tiles are butt-joint connected, as illustrated in **Figure 16** was chosen. The width of the aerogel tiles is critical as they must cover the 160° angle while still fitting into the space between the absorber tube and glass envelope of a PTR. The ideal aerogel dimensions are obtained, as shown in **Figure 16(a)**, and aerogels of ~ 150 mm length X 70 mm width are acquired from AeroShield to meet our design requirements. We must note that, as shown in **Figure 16(b)**, the absorber tube is designed to mount in a slightly off-center position in this test stand to facilitate the loading/unloading of the aerogels for repeated heat loss experiments. However, aerogels with current dimensions will still fit into a PTR receiver with a concentric configuration.

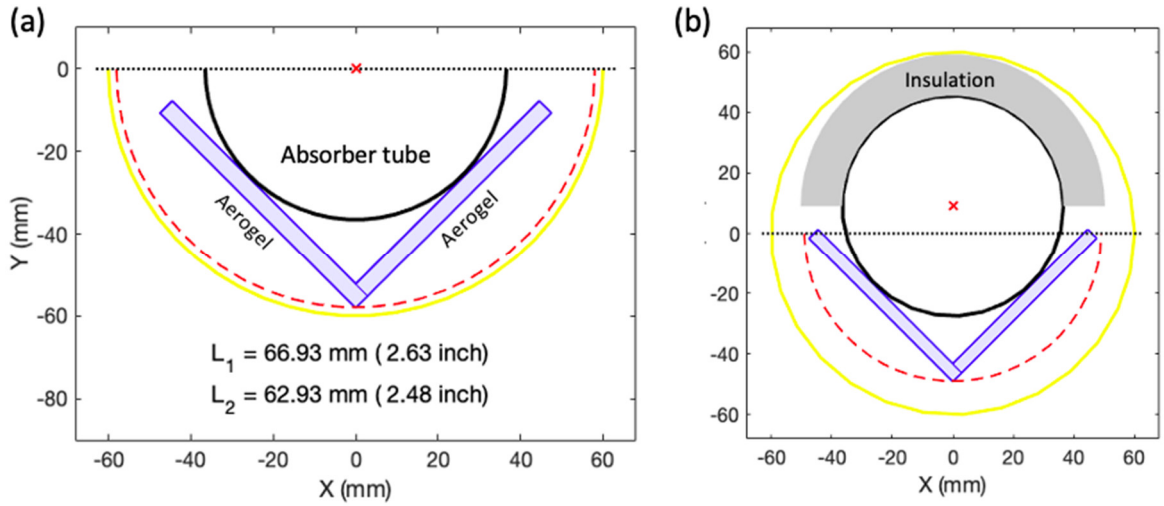

Figure 16. V-shape positioning of the aerogel tiles. (a) Required widths for aerogel tiles to cover the 160° angle and fit into the receiver are calculated. (b) The off-center positioning of the absorber tube creates more room for aerogel tiles and their tracks and facilitates repeated loading/unloading.

The V-shape geometry is beneficial as it simplifies the fabrication and design procedure with a marginal increase in thermal and optical losses. In fact, while the curved aerogels are ideal for insulating the absorber tube, our numerical model demonstrated that the optical losses associated with longer pathways through the aerogels in V-shape geometry in not significant. In addition, we realized that negligible thermal losses were added due to the gap between the aerogels and absorber tube in V-shape geometry.

The opaque insulations obtained for the test stand are half cylindrical shells as shown in **Figure 17(a)**. Small diameter rods are used as tracks to support the aerogel arrays along the tube. The absorber tube and the tracks are both supported by ceramic disks machined as shown in **Figure 17(b)**.

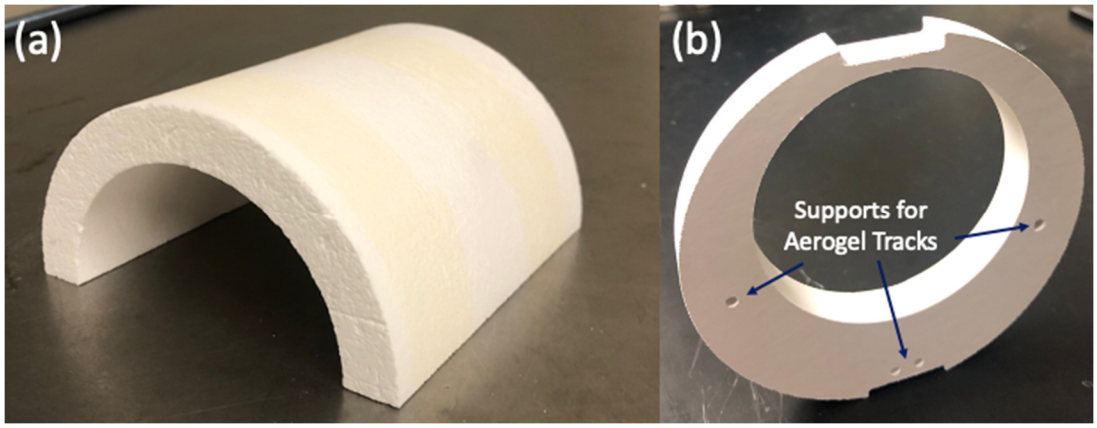

Figure 17. (a) Custom-made opaque insulating material with a half-cylindrical shell geometry is used to insulate the upper half of the absorber tube. (b) Small through holes to support the aerogel tracks are machined in the part. The tracks support the absorber tube within the glass envelope.

To maximize the receiver efficiency, the absorber tube is coated with a high-temperature-rated broadband absorbing coating. Note that only 160° of the absorber tube that would face the parabolic mirrors needs to be coated since there will not be any significant radiation hitting the remainder of the tube (**Figure 18(a)**). We also examined the effect of surface treatment on the heat loss performance of the absorber tube. Three stainless steel coupons including one with an untreated surface, one with bead blasted surface and one with bead blasted and polished surface were painted with the highly absorptive coating and baked for 72 hours at 700℃ in air. We subsequently performed FTIR and UV-Vis spectroscopies to compare their absorptance properties. As demonstrated in **Figure 18(b)**, a significant drop in absorptance of the surface treated samples in the short-to-mid wavelength of the IR region was observed. This is especially important as the absorber tube at 700℃ will dominantly emit at wavelengths within this range and a lower absorptance implies smaller emissivity and hence, less thermal losses. To verify this hypothesis, we inputted the obtained absorptance spectra for different surface treatments into our numerical model for receiver heat loss. The results, shown in **Figure 18(c)**, confirm that an absorber tube with a blasted and polished finish will have considerably lower heat losses than an untreated tube.

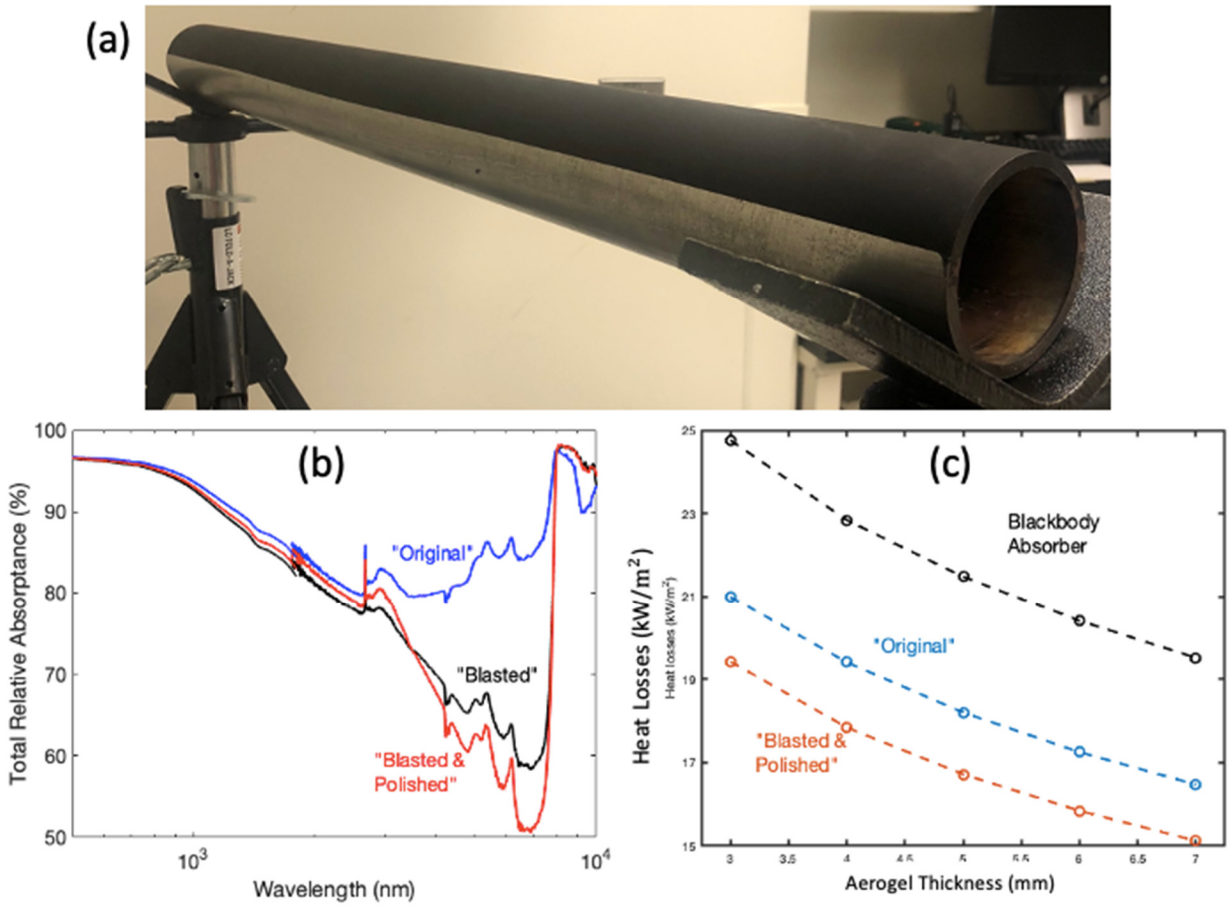

Figure 18. (a) Prepared absorber tube with 160° of its circumference coated with a high-temperature broadband absorptive paint, (b) Absorptance spectra for black painted stainless-steel samples with different surface treatments obtained by stitching FTIR and UV-Vis spectroscopy results, (c) Our numerical model predicts a significant decrease in heat losses for an absorber tube with a bead blasted and polished surface.

We also examined the stability of the high-absorptance coating at the operating temperature. Thermal stability is assessed by baking samples at 700°C for 72 hours and then at 800°C for 72 hours. While the bead blasted sample shows some degradation in form of flaking after being baked at elevated temperatures, both original and blasted and polished samples display thermal stability. We also evaluated the coating adhesion to the surface via the tape peeling test. As shown in **Figure 19**, coatings on both original and the blasted and polished samples demonstrate strong adhesion.

Figure 19. Images of black coated and baked stainless-steel coupons before and after the tape peeling test. Strong adhesion is observed as none of the grids are removed from the surface after the test.

An important aspect of our design is the integration of both opaque insulation and refractory aerogels into a PTR. Since the opaque insulation only covers the upper 180° of the absorber tube circumference (see **Figure 16 (b)**), and aerogels cover a 160° of the absorber tube, there is still a 10° uninsulated section on each side of the absorber tube. These small gaps are intentionally left open to preserve the fragile aerogels from any potential damages due to direct contact with hard opaque insulation blocks. Compliant wrapping insulation is, instead, designed to fill these gaps. **Figure 20** demonstrates how these three different insulations come together to fully insulate the absorber tube. To insulate the absorber tube, aerogels are mounted first. Compliant insulation cut to size is subsequently placed on the absorber tube and the opaque insulation blocks are pressed on top of the compliant strips to hold them in place. The elastic properties of the insulating strip allow its ends to spring back and fill the gaps between the top opaque insulations and the aerogel arrays, as depicted in **Figure 20**.

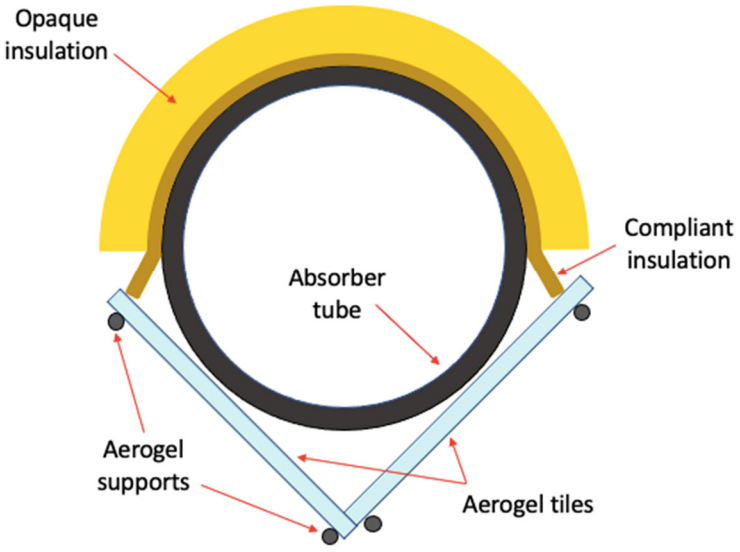

Figure 20. Demonstration of a fully insulated absorber tube using a combination of opaque and transparent insulating material for application in PTRs.

In addition to insulating the absorber tube, two thermal insulating blocks are also placed at both ends of the absorber tube (see **Figure 21**) to eliminate thermal losses from the edges. The main reason for using these thermal blocks is to increase the accuracy of the heat loss measurements. Hence, they will not be replicated in the PTR design. The thermal blocks will also function as thermal barriers to avoid overheating of the O-rings, flanges, and their sensitive attachments.

A resistive coil heater inserted into the absorber tube is another component of the test stand that differentiates between the test stand and a PTR. This heater allows for increasing the temperature of the absorber tube in the absence of concentrated solar radiation. **Figure 21** shows the developed PTR test stand with all required test equipment and instrumentation.

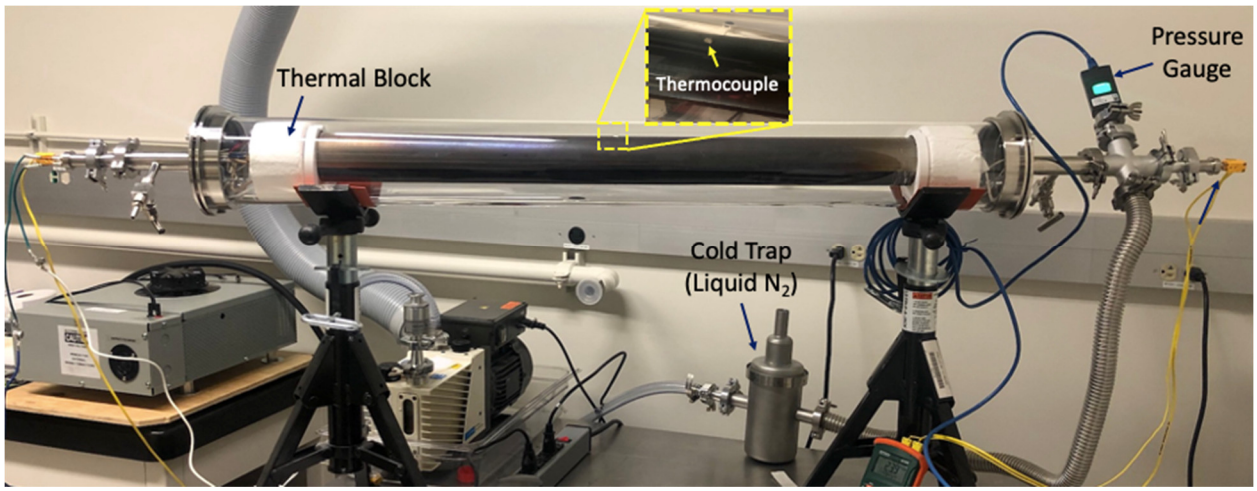

Figure 21. The developed PTR test stand with a 3-feet-long absorber tube for heat loss measurement experiments. Instrumentation for monitoring the receiver temperature and internal pressure is shown.

Instrumentation for the test stand:

Temperature of the absorber tube is monitored via two thermocouples installed near the middle of the tube, one attached to the bottom section of the tube and one inserted into the upper side, as shown in **Figure 21**. High-temperature resistant ceramic bond is used to fix and protect the thermocouple tips at their designated positions. Thermocouple and electrical feedthroughs (Ideal vacuum products) are used to extend the thermocouple and power wires outside of the sealed test stand and connect to a data acquisition system (Omega, OMB-DAQ-2408) and power supply, respectively. A high precision current probe (Fluke 80i-110s) is used to measure the current drawn by the heater to maintain a steady-state temperature. A variable AC voltage transformer (Variac by Staco) is used to supply a range of voltages across the resistive heater for different receiver temperatures. The Variac is equipped with plugs that connect to a digital multimeter to monitor the applied voltage. A dual-stage rotary vane pump (Agilent technologies, DS202) equipped with a liquid nitrogen cold trap in the foreline is used to evacuate the receiver chamber. A Pirani/capacitance diaphragm gauge (Agilent technologies, PCG752) is installed to monitor the receiver chamber pressure.

3.2. Variable temperature linear heat loss characterization

A resistive heater with a nominal resistance of $\sim 9.8\ \Omega$ inserted inside the absorber is used to control the tube temperature. At steady state, the power supplied to the heater must be equal to the power dissipated in the receiver test stand and lost to the ambient. The net amount of power supplied to the resistive heater (P) can be obtained as the product of the voltage applied across the coil heater (V in Volts), and current drawn by the heater (I in Amps). Power supplied per meter of the absorber tube (kW/m) is calculated by dividing P by the length of the absorber tube in our test stand.

Baseline experiments are run with an uninsulated absorber tube, similar to the setup shown in **Figure 21**. Another series of experiments are performed with only the upper half of the absorber tube being insulated (using the opaque insulation). A third set of experiments are executed with a fully insulated absorber tube where refractory aerogels are also integrated into the receiver. **Figure 22** shows the fully insulated receiver test stand undergoing heat loss experiments. It is worth noting that prior to carrying out the heat loss experiments, the chamber is purged with dry air to remove any moisture and then evacuated using a roughing pump.

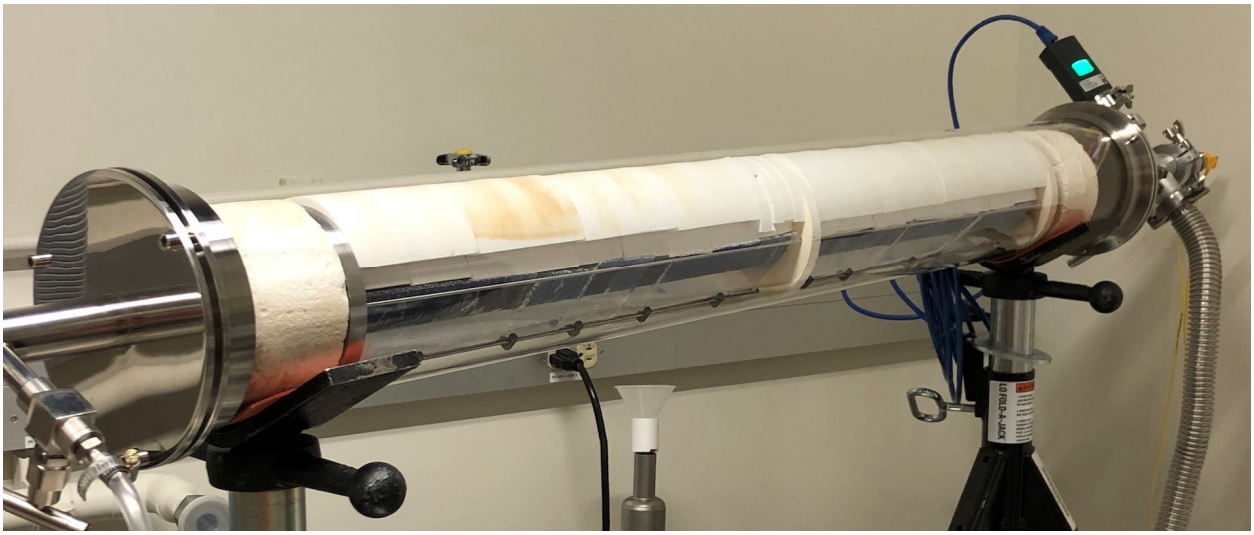

Figure 22. Picture of the AIR prototype in the thermal test stand.

Figure 23 shows the measured electrical power dissipated in the heater per unit absorber length over a range of absorber tube temperatures between 350℃ to 750℃ and for various insulation cases. The absorber tube temperature here is the average of two readings from thermocouples installed in the center of the tube (attached to the lower and upper walls). The linear power supply decreases significantly with the addition of both opaque (top) and transparent (bottom) insulation.

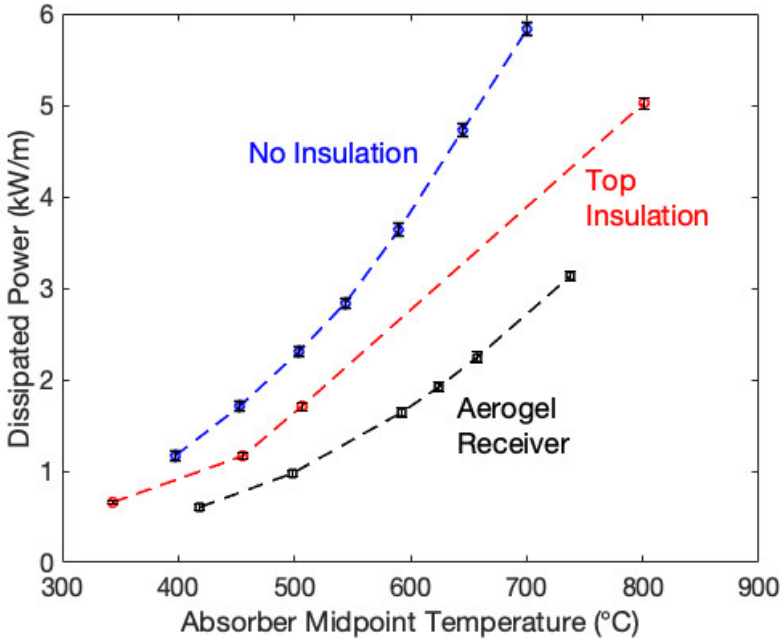

Figure 23. Power dissipated in (supplied to) the heater per unit absorber length versus the midpoint absorber tube temperature. Power input decreases substantially for the fully insulated aerogel receiver.

Uncertainty in heat loss measurement experiments can arise from a variety of potential sources including measurement instruments inaccuracy, variations in environmental parameters, and assumptions made in the analysis.

Since the power dissipated in the receiver follows P (Watts) = V (Volts) × I (Amps), the main instruments used to determine receiver thermal loss are current and voltage measurement tools. Our current clamp instrument is calibrated and reports current values with a maximum of $\pm$3% error. The voltages measured by a digital multimeter are discovered to be within $\pm$1% of the actual value, as well. The combination of these potential measurement errors is considered to calculate the uncertainty in thermal loss values resulted from the measurement tools. These uncertainties are shown with the vertical error bars in **Figure 23**. The small size of these error bars (< 4% of heat loss value) indicate insignificant uncertainty in thermal loss measurements.

While the power supplied to the heater is a measure of the receiver heat loss, this approach assumes thermal losses only occur radially, through the active area of the absorber tube which includes incident (bottom) and non-incident (top) areas. However, the test stand inevitably experiences thermal losses at both ends of the tube despite the efforts to eliminate them (i.e., the use of thermal blocks on both ends of the tube). These end (or edge) losses need to be subtracted from the measured power supplied to obtain the thermal loss through the active area of the receiver.

To translate the power dissipation measurements into linear heat loss values, we must account for the axial heat losses from the test stand. These losses are not negligible in our test stand because the ends of the receiver cannot be perfectly insulated due the measurement instrumentation and geometrical constraints. To this end, we estimate the axial heat losses, referred to as end losses, by comparing the results of our model to experiments for the evacuated baseline (uninsulated) case. The heat losses in this case are purely radiatively and easily described by a radiative heat transfer network. It should be emphasized that this model has no fitting parameters. The only inputs to the model are the experimentally determined thermal emittances of the coated and uncoated steel surfaces (c.f. **Figure 18**), the geometry of the tube, and the radiative properties of the glass envelope.

The model needs to account for the axial temperature profile along the length of the receiver. To account for this, we used readings from a third thermocouple installed near the edge of the tube (**Figure 24**). We then applied a parabolic temperature profile between the midpoint and edge temperatures to describe the axial profile. A parabolic profile is appropriate here because the axial heat diffusion equation includes a heat generation term that captures the difference between the dissipated electrical power and the outgoing thermal emission. The resulting temperature profiles are shown in **Figure 24.**

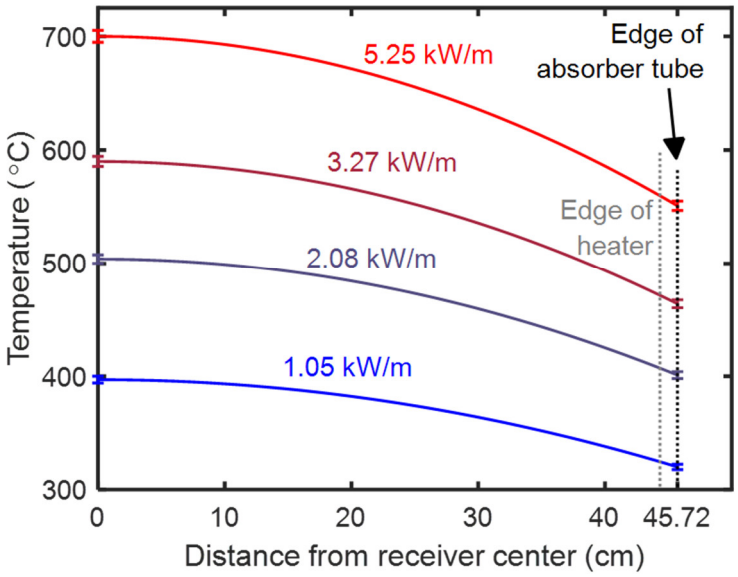

Figure 24. Parabolic profiles are used to approximate the temperature along the absorber tube based on temperature readings at the center and edge of the tube. Measured temperature profiles and power input values are shown for several steady-state experiments.

These parabolic temperature profiles were applied in our numerical model to improve the fidelity of the prediction. We then determined the end losses by taking the difference between the model-predicted heat loss values and the heater power measurements as a function of absorber tube temperature. **Figure 25** shows these end losses as a function of absorber tube edge

temperature. Importantly, the edge losses are only a function of the edge temperature and can therefore be applied the other receiver configurations.

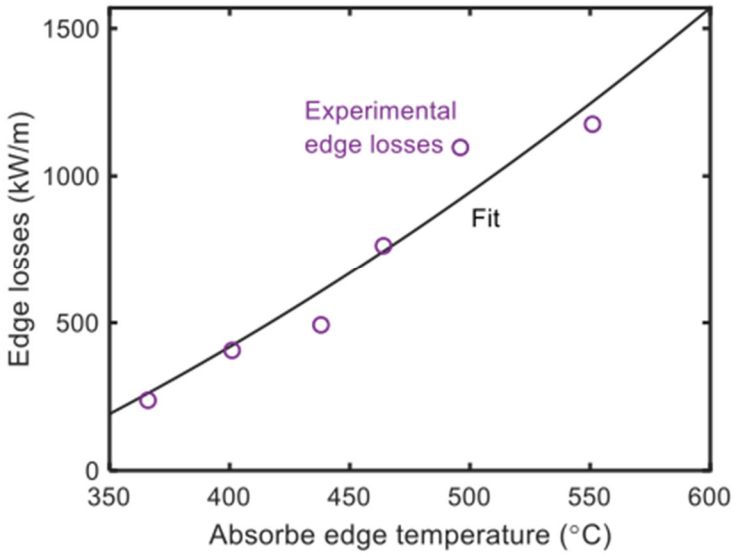

Figure 25. Parasitic heat losses from the ends of the absorber tube determined as a function of absorber tube edge temperature.

Figure 26 shows the temperature dependence of the linear heat losses from the active receiver area after accounting for the end losses and the non-uniform temperature profile. The agreement between the experimental and predictions for heat losses for the aerogel insulated receiver is excellent. The procedure for determining the end losses could be further validated through additional experiments. Nonetheless, the linear heat loss at 700℃ for the V-shaped prototype AIR is about 1650 W/m, which represents a significant reduction (>50%) relative to the baseline case.

Lastly, we note that variation in receiver chamber pressure is a factor that could contribute to disagreement between model and experiment. During the baseline experiments with the uninsulated tube, the chamber pressure increased from 30 to 150 mbar as the operating temperature was raised from 350℃ to 750℃. Meanwhile, the pressure range varied between 110 to 290 mbar for the fully insulated receiver. The pressure increase is primarily caused by the introduction of the high surface area aerogels into the test stand. While variation in chamber pressure can result in changes in non-radiative thermal losses, our model indicates minimal sensitivity of thermal losses to the chamber pressure.

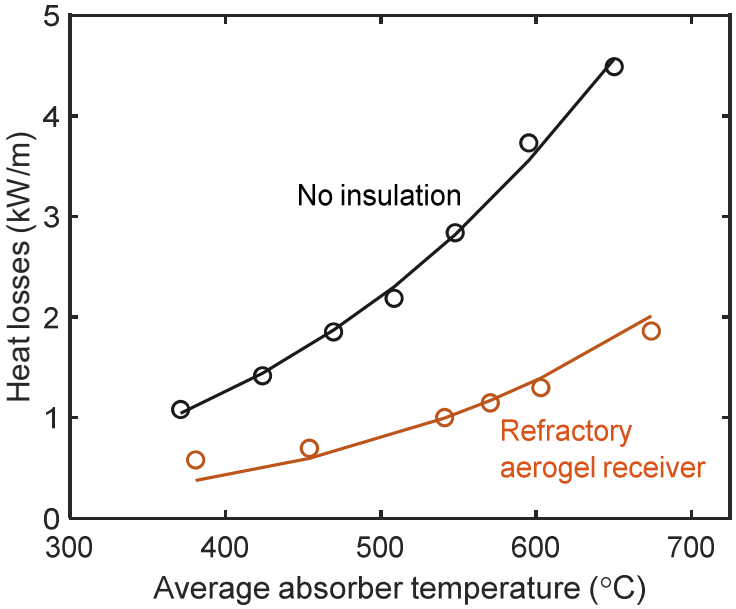

Figure 26. Experimental heat loss values and model predictions after accounting for non-uniform temperature profile and end losses. Receiver chamber pressure held between 30-300 mbar.

Summary:
The combination of low uncertainty in the power dissipation measurements (<5%) and an absorber tube temperature range that exceeds 700°C **fulfills milestone 3.1.** Meanwhile, the agreement between model predictions and measured heat losses is within 5% **which fulfills milestone 3.2.** Overall, these experimental results establish a new milestone for high-temperature linear receiver heat-loss performance and demonstrate that the integration of aerogels can lead to practical gains in performance of established receiver technologies. Furthermore, the experimental validation of the model is noteworthy because the model shows that there is substantial room for further improvement in performance.

3.3. Observed failures and opportunities for improvement

Improvements to the aerogel insulated receiver have been made during the development and assembly process and further improvements are still needed. Sagging of the stainless-steel rods used as aerogel supports was one of the failures observed during our first assembly attempt. The sagging led to the supports touching the quartz tube during the assembly. This interaction resulted in displacement and crowding of aerogel tiles. The design was improved by adding an extra disk near the receiver midpoint to provide additional support for the tracks.

Small gaps between the aerogel tiles were also noticed in the assembled insulated receiver. The presence of these gaps can result in increased thermal losses especially if operated in ambient.

Improved performance can be obtained by utilizing a mechanism to keep the aerogel tiles closely packed.

It is important to anneal refractory aerogels in air prior to their exposure to high temperatures in vacuum. In the first set of heat loss measurement experiments under vacuum, freshly coated refractory aerogel tiles turned black after testing the receiver performance at elevated temperatures. This phenomenon occurs due to the presence of residual ALD precursor in the aerogels. Blackened aerogels were regenerated after being annealed in air as the carbon reacted with oxygen and formed gaseous carbon dioxide.

In this work we used ceramic fiber strips as the compliant insulating material. While the insulation is rated for 2300°F, the binder used in the insulation burns off at temperatures between 600-800°F. Burning of the binder releases substances that can be deposited on the surrounding surfaces if proper ventilation is not sustained. In our first run of receiver testing with these flexible insulations, we noticed a dark brown material deposited on areas of the quartz tube as well as the top insulation shells. The deposited material appears to be the product of burning the insulation binder. For the following experiments, we heated the insulation in a muffle furnace to a temperature above 800°F prior to placing them in the receiver test stand.

There is still room to improve the vacuum level of the receiver, as well. To achieve an ideal vacuum with a receiver pressure of less than 100 mTorr at 700°C, removing the chamber moisture is essential. Purging of the chamber at high temperature with N2 or dry air is expected to effectively remove the moisture. Shortening the vacuum hoses can also help improve the vacuum level.

4. Techno-economic analysis

Outcomes:
Developed and validated in-house models for annualized energy production and LCOE.
Aerogel based receiver, operating at solar salt temperatures, are predicted to lower LCOE by 5% relative to baseline while not requiring vacuum.

Milestone #	Performance Metric	Success Value	Assessment Tool / Method of Measuring Success Value	Verification Process	Additional Notes
EOP	LCOE or Annualized Energy Production	≥ 10% improvement relative to a reference Comparison made between a) Gen3 fluid system; b) commercially available system.	**Min %**. Comparisons made on the basis of overall plant energy efficiency, annualized energy production, LCOE; calculated based on measured parameters. High-T (Gen3) comparisons are pending availability of system-level cost and efficiency models.	Report sent to DOE for verification. Data format: overall and constituent efficiencies, throughputs, LCOE ($/kWh); sensitivity to major plant design parameters (e.g., field size).	Receiver input parameters refined over the course of the project as measured properties and cost estimates become more reliable. When switching power cycles, change one variable at a time.

4.1. Annualized energy production and LCOE model formulation

We have developed an in-house LCOE model to estimate the cost of an CST plant primarily because NREL's System Advisor Model (SAM) is currently incapable of modeling high temperature linear receiver plants. Rather, we use a more rudimentary economic model, the fixed charge rate (FCR) analysis:

$$LCOE = \frac{TCC * FCR + FOC}{AEP} + VOC \tag{5}$$

where TCC is the total capital cost, FCR is the fixed charge rate, FOC is the fixed operating cost, AEP is the annualized energy production, and VOC is the variable operating cost. The TCC is calculated using a framework developed by Asegun Henry and Ravi Prasher[14], where the subtotal cost of a CST plant is the sum of its four major components:

$$SCC = SM\frac{C_{field}}{G_s \times \eta_{S-E}} + SM\frac{C_{receiver}}{\eta_E} + t_{storage}\frac{C_{storage}}{\eta_E} + C_{cycle} \tag{6}$$

$$TCC = y(SCC + xSCC) + xSCC + SCC$$

(7)

where SM is the solar multiple, C_i is the cost of the solar field (i.e., collectors), receivers and heat exchanger system, thermal storage, and power cycle, Gs is the solar incidence design point, $t_{storage}$ is the hours of thermal storage, and η_{S-E} is the solar to thermal efficiency, and η_E is the efficiency of the power cycle. Equation 3 then converts SCC to TCC by accounting for indirect costs (first term) and contingency costs (second term). The values for SM, $t_{storage}$, η_E, and C_i are taken from the 2012 SETO Sunshot Vision study, and the 2020 Sunshot targets are used (**Table 9**). The only parameter that changes with the aerogel-based receiver is $C_{receiver}$, which needs to account for the cost of the aerogel tiles which we assume is $17/L per a cost estimate from the aerogel tile providers, Aeroshield. We assume the cost of the ALD coating process is dominated by material costs, primarily trimethylaluminum. As a conservative estimate, we assume the processing and handling costs of the ALD process is twice that of the material costs. Even with the additional costs, the cost of the solar receiver only increases by ~5%. Therefore, for the aerogel-based receivers, we increase $C_{receiver}$ by 5%.

Table 9. Inputs to the LCOE model

Input	Value
Site preparation	$20/m^2
Solar field (e.g., collectors)	$140/m^2
Heat transfer system (e.g., receivers, HEX)	$9.5/m^2
Thermal energy storage	$15/kW$_{th}$
Cost of the power cycle	$880/kW$_e$
Hours of storage	12
Power cycle efficiency	0.47 (550C) 0.51 (700C)
Solar multiple	2.8
DNI design point	1000 W/m^2
Annualized optical efficiency	72.1%

The two remaining terms that need to be computed are AEP and η_{S-E} which are both a function of plant performance. The overall plant efficiency is a function of the efficiency of each of the components in Equation 2:

$$\eta_{plant} = \eta_{optical} * \eta_{receiver} * \eta_{storage} * \eta_E \quad (8)$$

We chose the Solar Dynamics parabolic trough as the collector which as an annualized optical efficiency, $\eta_{optical}$, of 72.1%, and the storage efficiency is assumed to be 95%[15]. Finally, this leaves the receiver efficiency (see Equation 4) as a key output of the technoeconomic model. For the aerogel-based solar receiver, we assume a solar-weighted transparency of 97% for the glass tube and use the experimentally determined solar-weighted transparency of 95% for the refractory aerogel. Lastly, we use the verified model from Section 3.2 to estimate the heat losses of an ideal aerogel receiver, one fitted with curved aerogels (rather than the V-shape).

To estimate the annualized receiver efficiency, we estimate the receiver efficiency over the course of a "typical" day in the Phoenix, AZ region (**Figure 27**). The average direct normal irradiance (DNI) is 7.5 kWh/m^2. One issue with parabolic trough collectors is that the heat transfer fluids may freeze at night, but we account for this by assuming electrical resistive heaters maintain the temperature of the receivers at a minimum temperature of 200°C, which is above the melting point of chloride salts (~150°C). The temperature of the receiver only increases when the solar DNI exceeds the thermal losses of the receiver (**Figure 27**). Furthermore, the thermal losses are also averaged along the length of the solar collector loop. The temperature difference between the inlet and outlet of the loop is provided by SAM, which supplies temperature gradients for various power cycle temperatures. The receiver efficiency is then the sum of the of absorbed solar energy minus the heat lost over the course of the day, and the AEP is a product of the yearly heat collected and the plant efficiency.

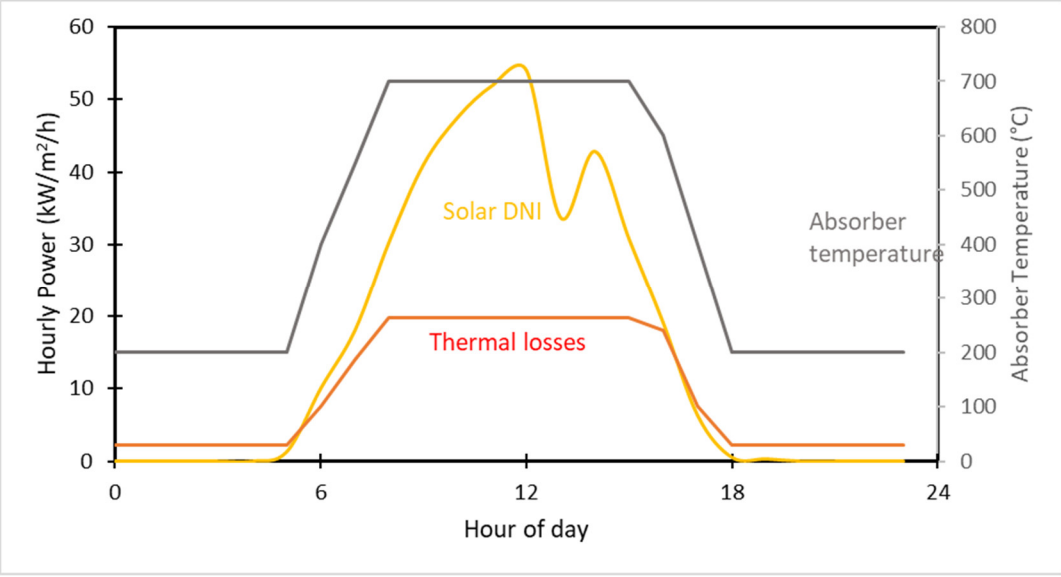

Figure 27. Temporal temperature and solar incidence for the receivers. The temperature of the receiver only increases when the solar DNI exceeds the thermal losses at any temperature.

4.2. Model validation and results

To first confirm that the LCOE model is accurate, we used a variety of cost inputs and design parameters and compared the values to the 2012 Sunshot Visions report (**Table 10**). The in-house

model is accurate since it estimates the LCOE of the plant designs within 1.5% of references. Therefore, we can confidently proceed with the in-house model.

Table 10. Validation of In-house LCOE model

	2010 Trough	2020 Trough Roadmap	2020 Sunshot Targets (550°C tower)
SETO values	20.40	11.60	6.00
In-house model	20.01	11.43	6.05

The cost results for the updated CST plants integrated with aerogel-based receivers is provided in **Table 11**. We model the aerogel receiver at both 550°C and at 700°C for moderate and high temperature sCO_2 cycles. As a baseline, we provide a cost for a receiver that uses selective absorbers at 400°C. These include updated cost projections from a recent NREL CSP cost survey report. Recent cost reductions in the cost of the solar field (from \$190/m^2 to \$140/m^2) are the primary reason for the lower cost. The first takeaway from this analysis is that the refractory aerogel receiver, at both 550°C and 700°C, even with the curved aerogel shape, is costlier than the selective absorber design at 400°C. This is primarily due to the relatively high effective emissivity of the current refractory aerogels (~0.35), which are not plasmonic (i.e., do not leverage PEGS). The refractory aerogel receiver performs well at peak irradiance (550°C and ~50 suns), but the heat losses at night lead to its higher LCOE overall. Similarly, the heat losses at 700°C are currently too high to justify using linear receivers.

However, there is some potential with tandem receivers, i.e., combining a non-plasmonic refractory aerogel with a state-of-the-art selective surface rather than a broadband absorber. For 550°C, we use the same spectrally dependent selective absorber properties as the 400°C (CIEMAT), and at 700°C, we use the nanoparticle-based paint absorber recently developed[16] by Jifeng Liu's group at Dartmouth. Combining selective absorbers and aerogels leads to the lowest heat losses at night, so despite the loss in solar absorptance, the tandem receiver offers the greatest potential for higher temperature linear receivers. Specifically, the cost reduction from the 400°C baseline case to the 550°C tandem receiver is 6.3%. Integration of plasmonic aerogels or selective surfaces specifically designed for use in tandems is expected to further lower LCOE. This is a promising avenue for further investigation, beyond of the scope of this LCOE study which is based on materials demonstrated at the receiver prototype scale.

Table 11. LCOE and LCOH of various prospective plant design

	Selective absorber (400°C)	Refractory aerogel (550°C)	Tandem receiver (550°C)	Refractory aerogel (700°C)	Tandem receiver (700°C)	Solar PV with storage
LCOE (¢/kWh)	8.63	9.33	8.09	13.5	10.91	8.50 (battery)
LCOH (¢/kWh$_{th}$)	1.91	2.10	1.79	2.96	2.44	4.33 (TES)
Annualized efficiency (%)	21.2	19.9	21.7	15.8	18.0	-

Regardless of the higher costs of electricity production, the refractory aerogel receiver has the potential to offer very low-cost high-temperature heat for industrial processes. The primary way to decarbonize an industrial heating process is to use solar PV with thermal energy storage (TES), but that approach is relatively expensive at 4.33 ¢/kWh$_{th}$. In contrast, the cost of high temperature heat from tandem receivers is only 1.79 and 2.44 ¢/kWh$_{th}$ at 550 and 700°C, respectively.

4.3. Sensitivity analysis

To understand which properties of the receiver have the biggest impact on LCOE, we developed a sensitivity plot for the 550C tandem receiver plant (**Figure 28**) using the inputs shown in **Table 9** as the baseline scenario. **Figure 28** shows, as expected that decreasing receiver and storage costs will lead to lower LCOE, but the sensitivity is quite low. Rather, reducing the cost of the power cycle and solar field are the most critical cost measures to reducing the overall LCOE. Notably, however, the LCOE is highly sensitive to the performance of the receiver. Specifically, an aerogel with 10% lower solar transparency increases the LCOE to ~9.9 ¢/kWh (we note that the refractory aerogel is already 95% transparent, so the blue bar for aerogel transparency is not entirely physically meaningful). The thermal losses also have a significant impact because a 10% decrease in heat losses would decrease the LCOE by ~0.4 ¢/kWh. This sensitivity analysis shows that methods to increase the performance of the refractory aerogel receiver, despite their increase in the cost of the receiver, will likely lead to large reductions in the overall LCOE of the plant. Such methods include incorporating selectively transparent plasmonic nanoparticles.

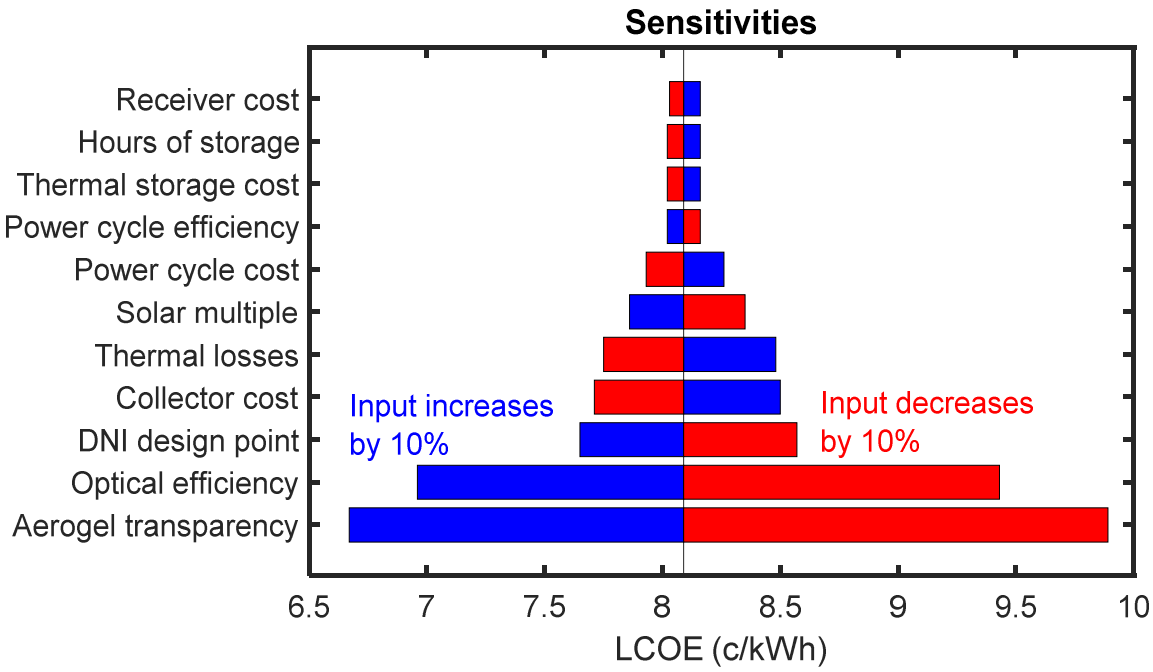

Figure 28. Sensitivity analysis of the tandem receiver plant at 550C.

Inventions, Patents, Publications

Journal Articles:

(1) Andrew J. Gayle, Zachary J. Berquist, Yuxin Chen, Alexander J. Hill, Jacob Y. Hoffman, Ashley R. Bielinski, Andrej Lenert, Neil P. Dasgupta; "Tunable Atomic Layer Deposition into Ultra-High-Aspect-Ratio (>60,000:1) Aerogel Monoliths Enabled by Transport Modeling", Chemistry of Materials, 33, 14, 5572, 2021.

(2) Zachary Berquist, Andrew J. Gayle, Neil P. Dasgupta, Andrej Lenert, "Transparent Refractory Aerogels for Efficient Spectral Control in High Temperature Solar Power Generation"; Advanced Functional Materials, 2021.

Conference Presentations:

(1) Andrew J. Gayle, Zachary J. Berquist, Yuxin Chen, Alexander J. Hill, Jacob Y. Hoffman, Ashley R. Bielinski, Andrej Lenert, Neil P. Dasgupta, "Tunable ALD Infiltration into Ultra-High-Aspect-Ratio Aerogels Enabled by Process Modeling for High-Temperature Solar Thermal Applications", 21st International Conference on Atomic Layer Deposition, June 27-30, 2021.

(2) Andrew J. Gayle, Zachary J. Berquist, Yuxin Chen, Alexander J. Hill, Jacob Y. Hoffman, Ashley R. Bielinski, Andrej Lenert, Neil P. Dasgupta, "High-Temperature Stabilization of Silica Aerogel Monoliths Using Model-Enabled Conformal Atomic Layer Deposition", ES2021/SHTC2021, June 16-18, 2021.

(3) Ali Davoodabadi, Zachary J. Berquist, Andrew J. Gayle, Neil P. Dasgupta, Andrej Lenert, "Experimental Demonstration of High-Efficiency Refractory Aerogel-Integrated Linear Receiver for Concentrating Solar Power", ES2022/SHTC2022, July 11-13, 2022.

(4) Zachary J. Berquist, Andrej Lenert, "Modeling the Efficiency of an Ambient Pressure, Mesoporous Silica-Based Linear Receiver for Parabolic Trough Collectors", ES2022/SHTC2022, July 11-13, 2022.

Patents:

Andrej Lenert, Neil P. Dasgupta, Zachary J. Berquist, Andrew J. Gayle, "TRANSPARENT MESOPOROUS MATERIALS AND DEVICES COMPRISING SAME"

Path Forward

Our work to date, through two SIPS projects, has focused on initial de-risking of refractory aerogels. These SIPS projects addressed three specific risks (Table 12) that were deemed highly important: (i) potential loss of mesoscale porosity, which is critical to the optical and heat-insulating properties of the aerogels, (ii) potential loss of insulation value due to dehydroxylation and water desorption at high temperatures, which results in a large transmittance window below 5 µm in conventional silica aerogels (this IR window accounts for ~63% of the blackbody emitted power at 700°C), and (iii) inability to translate the materials into performance gains within practical trough configurations. These initial challenges have been overcome by the U-M team, respectively, through the development of a model-predictive ultrahigh aspect ratio (UAR) ALD process that produces a refractory oxide throughout the aerogel, incorporation of IR-plasmonic ITO nanoparticles within the aerogel matrix, and development of a prototype receiver featuring a segmented array of aerogel tiles which validated the anticipated performance predictions.

Table 12. Trajectory of the refractory aerogel technology, including results from SIPS support.

Concept	Initial Innovation	Initial Risk	Accomplishment	Remaining Risk
Transparent mesoporous refractory insulation for black receivers	Receiver does not require a low-emittance absorber coating or high vacuum to maintain efficiency	Loss of porosity and insulation value at Gen3 temperatures. Poor translation to practical receivers.	+Refractory monolayer coating stabilizes pores up to 800°C +Added ITO particles maintain ultrahigh heat insulation +36-inch prototype development and Receiver efficiency model validation	+Demonstration of a "production" prototype +Mechanical design and durability in an integrated receiver

By overcoming the thermal stability and selectivity challenges, the refractory insulation approach provides a path toward leveraging the unique advantages of mesoporous TIMs in PTCs: (i) the receiver does not require a solar absorbing surface with low thermal emittance, and (ii) operation at moderate vacuum levels (~10 mbar) can be tolerated. For lack of stable coatings and perfect hermetic seals, the above advantages are critical to achieving and maintaining performance over the lifetime of the plant. High vacuum levels (~10^{-3} mbar) used in current PTCs are prone to breakdown, mainly due to mechanical faults and outgassing, which leads to shorter lifetimes and costly O&M. Stratified air cavities, on the other hand, provide negligible resistance to outgoing re-radiation and lose more heat when tilted. In contrast, our approach offers ultrahigh, tilt-insensitive thermal resistance at pressures up to 10 mbar. This represents a 3-4 order of magnitude increase in operating pressure which offers performance and cost advantages. It allows the receiver to maintain performance over the lifetime of the CSP plant, in line with SETO goals. Furthermore, the higher pressure makes it possible to potentially design a lower-cost vacuum tube that is re-sealable. This would also allow for the replacement of cracked or broken aerogel segments if deemed necessary.

Funding is now critical to address the remaining mechanical, manufacturing, and commercial adoption risks. The curved aerogel design is critical to high receiver efficiency. In comparison to flat aerogels, our simulations show that curved aerogels have a ~10% higher receiver efficiency because they minimize the outer surface area of the refractory insulation which governs heat losses.

References

1. Gayle, A. J. *et al.* Tunable Atomic Layer Deposition into Ultra-High-Aspect-Ratio (>60000:1) Aerogel Monoliths Enabled by Transport Modeling. *Chemistry of Materials* **33**, 5572–5583 (2021).
2. Lenert, A., Berquist, Z. J. & Turaczy, K. K. Plasmon-enhanced greenhouse selectivity for high-temperature solar thermal energy conversion. *ACS Nano* **14**, 12605–12613 (2020).
3. Berquist, Z. J. *et al.* Transparent Refractory Aerogels for Efficient Spectral Control in High-Temperature Solar Power Generation. *Wiley Online Library* **32**, (2021).
4. Carrillo, A. J., González-Aguilar, J., Romero, M. & Coronado, J. M. Solar Energy on Demand: A Review on High Temperature Thermochemical Heat Storage Systems and Materials. *Chemical Reviews* **119**, 4777–4816 (2019).
5. Thiel, G. P. & Stark, A. K. To decarbonize industry, we must decarbonize heat. *Joule* vol. 5 531–550 Preprint at https://doi.org/10.1016/j.joule.2020.12.007 (2021).
6. Tagle-Salazar, P. D., Nigam, K. D. P. & Rivera-Solorio, C. I. Parabolic trough solar collectors: A general overview of technology, industrial applications, energy market, modeling, and standards. *Green Processing and Synthesis* vol. 9 595–649 Preprint at https://doi.org/10.1515/gps-2020-0059 (2020).
7. Kincaid, N., Mungas, G., Kramer, N., Wagner, M. & Zhu, G. An optical performance comparison of three concentrating solar power collector designs in linear Fresnel, parabolic trough, and central receiver. *Applied Energy* **231**, 1109–1121 (2018).
8. Zhang, K. *et al.* A review on thermal stability and high temperature induced ageing mechanisms of solar absorber coatings. *Renewable and Sustainable Energy Reviews* **67**, 1282–1299 (2017).
9. Zhao, L. *et al.* Harnessing Heat beyond 200 °c from Unconcentrated Sunlight with Nonevacuated Transparent Aerogels. *ACS Nano* **13**, 7508–7516 (2019).
10. Strobach, E., Bhatia, B., Yang, S., Zhao, L. & Wang, E. N. High temperature stability of transparent silica aerogels for solar thermal applications. *APL Materials* (2019) doi:10.1063/1.5109433.
11. Lenert, A., Dasgupta, N., Berquist, Z. & Gayle, A. Robust and Spectrally Selective Aerogels for Solar Receivers. (2021).
12. Stettenheim, J., McBride, T., Brambles, O. & Johnson, L. Design and Field Testing of Manufacturable Advanced Low-Cost Receiver for Parabolic Trough Solar Power. (2019).
13. Burkholder, F. & Kutscher, C. Heat Loss Testing of Schott's 2008 PTR70 Parabolic Trough Receiver. (2009) doi:10.2172/1369635.
14. Henry, A. & Prasher, R. The prospect of high temperature solid state energy conversion to reduce the cost of concentrated solar power. *Energy & Environmental Science* **7**, 1819–1828 (2014).
15. Turchi, C., Boyd, M., Kesseli, D., Kurup, P. & Mehos, M. CSP systems analysis-final project report. (2019).

16. Wang, X., Lee, E., Xu, C. & Liu, J. High-efficiency, air-stable manganese–iron oxide nanoparticle-pigmented solar selective absorber coatings toward concentrating solar power systems operating at 750 °C. *Materials Today Energy* **19**, 100609 (2021).